UILU-ENG 84-3602

Report No. 102

LASER PROCESSING OF CAST IRON FOR ENHANCED EROSION RESISTANCE

by

CHUNG-HSIN CHEN
Department of Metallurgy and Mining Engineering, UIUC

A Report of the
MATERIALS ENGINEERING - MECHANICAL BEHAVIOR
College of Engineering, University of Illinois at Urbana-Champaign
February 1984

ABSTRACT

The surfaces of nodular and pearlitic gray cast iron specimens have been modified by CO_2 laser processing for enhanced hardness and erosion resistance. Control of the microstructure was primarily achieved by controlling the processing parameters of laser beam interaction time and power density. The typical laser beam interaction times and power densities used in these experiments were 1.5 sec, 500 kW/cm^2 for focused beam laser processing.

Examination of the laser processed near-surface layer showed considerable increase in microhardness and a greatly refined microstructure. Microstructural and microchemical analyses were done using optical microscopy, scanning and x-ray diffraction. There are two kinds of microstructures in the laser hardened layer--a feathery microstructure with a higher hardness (DPH 945 to 1245) and a dendritic microstructure with a lower hardness (DPH 560 to 940).

Erosion testing was done by using a water slurry (SiO_2 or SiC) abrasive system. Weight loss measurements and erosion crater profiles were used to evaluate erosion resistance of the various microstructures. In general, both ductile and gray cast iron samples showed more quantitative improvement in erosion resistance after laser processing.

ACKNOWLEDGEMENT

The author would like to express his sincere gratitude to his advisors, Professor C.J. Altstetter and Professor J.M. Rigsbee for their abundant guidance and assistance with this work.

The support of the facilities of the University of Illinois is acknowledged, including those of the MRL, MERL and especially the Department of Metallurgy and Mining Engineering.

The author acknowledges the support of the Caterpillar Tractor Company, which provided sample materials.

The help of the staff of the Department of Metallurgy and Mining Engineering is acknowledged, including the assistance of Mr. Everett Heiser for the machine shop work and Debbie Davis for typing this thesis.

Thanks is due also to Jon Culton and Tom Casales for their assistance with the laser and its operation.

Most of all, the author is greatly indebted to his wife Tzu-Lin, his family and Dr. C.T. Wei for their constant encouragement and consideration.

The author gratefully acknowledges the support of the Department of Energy, Office of Coal Utilization through the Materials Engineering Research Laboratory, contract # DE-AC02-78-ER-10004.

TABLE OF CONTENTS

CHAPTER PAGE

LIST OF TABLES

LIST OF FIGURES

FIGURE PAGE

I. INTRODUCTION

A. Statement of the problem

Cast irons are common materials used because of their low cost and superior properties--low melting point, good fluidity and castability, excellent machinability, good wear resistance and good mechanical properties. However, under some severe service condition their performance and reliability are limited by various forms of wear, which can cause frequent shutdown of equipment for replacement of worn castings and a consequent increase in the total cost for their use.

One way of minimizing these troubles is to use more highly alloyed materials which combine superior wear resistance with adequate toughness. This solution to the problem is achieved only by increased consumption of scarce alloying elements and increased material cost. Generally manufacturing procedures also become more exacting and costly.

An alternative to the use of more alloying is to change processing techniques to modify the microstructure in such a way as to improve erosion resistance. One means of doing this is selective surface hardening. The CO_2 laser is a remarkably versatile surface hardening tool since it allows precise spatial and temporal control of the energy delivered to a surface. These characteristics allow surface processing to be done with speed, minimal distortion, no need for quenchant, the ability to treat hard-to-reach places and only those places where it is needed, and limited expenditures of energy. It is likely that in many instances a controlled surface hardening technique such as laser processing will provide a better alternative than alloying or through-hardening as far as wear resistance and total cost are concerned.

B. Research Objective

The objective of this research is to improve the wear (erosion) resistance of cast iron by laser surface treatment and to correlate the enhanced erosion resistance with the laser-induced microstructural changes. Two types of commonly used cast irons--pearlitic gray iron and ductile nodular iron with a pearlite/ferrite matrix were examined, both before and after laser treatment. The original microstructures, the laser hardened microstructures and the hardnesses were correlated with the laser processing parameters and wear properties.

II. LITERATURE SURVEY

A. Laser and its applications

A laser produces a highly collimated beam of coherent monochromatic radiation with wavelengths ranging from optical to infra-red [1]. Because of its high degree of coherency and collimation a laser beam can be focussed to a small diameter creating power densities as high as $10^9 W/cm^2$. Based on the power density and beam interaction time, a laser can be very effective in metalworking operations involving heating, melting or cutting.

In general, most metals absorb only a small fraction of the incident laser beam energy at infra-red wavelengths (1-1000 μm). However, as the wavelength decreases, the normal spectral absorptance increases greatly [2], as shown in figure 1 for iron. It is also observed that absorption increases gradually for a solid metal as the surface temperature increases and that absorption increases dramatically upon melting. Figure 2 illustrates this phenomenon and correlates it with the effect of increasing beam power density [3]. Below a threshold of 1.5×10^4 watts per square centimeter, uncoated metal surfaces typically absorb less than 10 percent of the incident beam energy at the 10.6 μm wavelength radiation characteristic of a CO_2 laser (coated surfaces can absorb 90 percent of the energy). This power density region is therefore suitable for heat treatment where melting is not desired. Between a power density of 1.5×10^4 to 1.5×10^6 W/cm^2, melting can occur with the absorption increasing to between 60 and 90 percent of the incident beam energy. It is in this range that metal welding is accomplished. Above a power density of 1.5×10^6 W/cm^2, metals begin to vaporize under the laser beam and may then be cut.

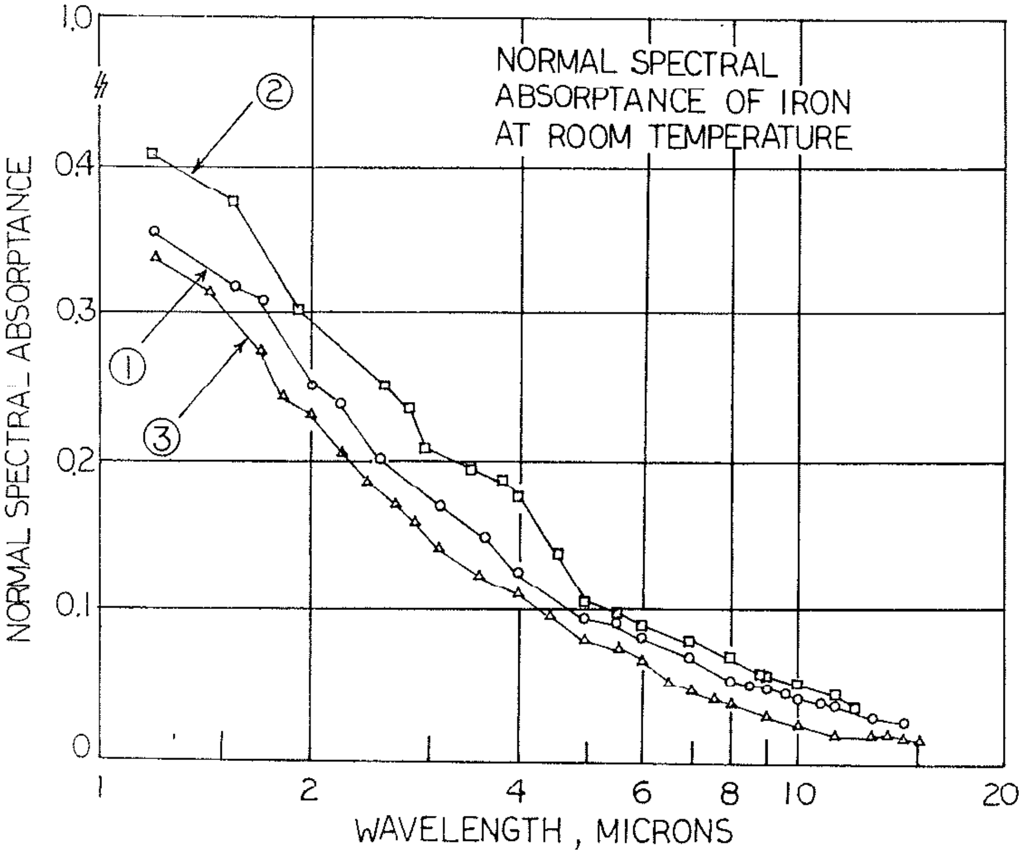

Figure 1. Normal spectral absorptance of iron at room temperature.
1) mechanically polished and cleaned
2) mechanically polished and cleaned, heated at 1058°K for 2 1/2 hrs and at 1316°K for 5 hrs.
3) measured after emissivity determination [2].

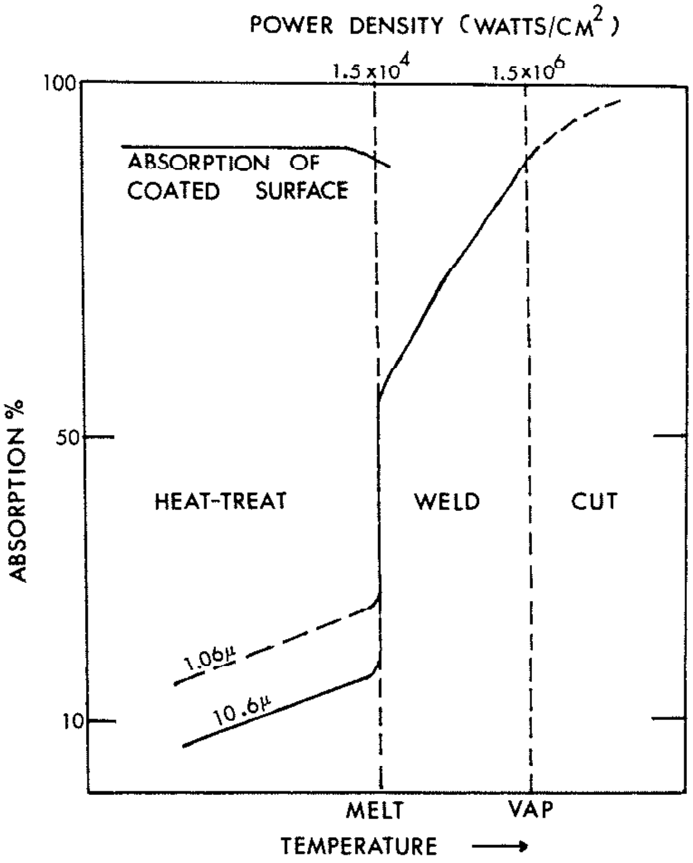

Figure 2. Absorption in metals vs. power density at two different wavelengths [3].

The temperature rise induced in a material by laser irradiation depends both on the thermophysical properties of the material and on the energy-time characteristics of the focussed laser output [4]. The optical properties characterizing the metal surfaces are the absorptance, α, and reflectance, R_o. A portion of the incident laser intensity, I, is absorbed by the metal within its electromagnetic skin depth, typically 10-100 nm, and is converted into heat. The heat rapidly diffuses away from this near surface region to depths given by the thermal diffusion length, $(2Dt_p)^{1/2}$, where t_p is the dwell time or pulse time of the laser and D is the thermal diffusivity. The value for thermal diffusivity is given by the relation $D = K/C\rho$, where K, C and ρ are the thermal conductivity, specfic heat, and density, respectively. For a square-wave laser pulse, the average temperature rise within this thermal diffusion layer is:

$$\Delta T = \frac{(1-R_o)It_p}{C\rho(2Dt_p)^{1/2}}$$

Following irradiation the heat is rapidly absorbed by the bulk of the solid, the self-quenching times being on the order of t_p. For $\Delta T = 1000$ K, quench rates of $10^5 - 10^{10}$ K /sec are possible for exposure times of $10^{-3} - 10^{-9}$ sec. If the energy input is sufficiently high, melting will occur from the surface to some fraction of the thermal diffusion length.

Lasers can be classified according to the lasing medium as solid state, liquid or gas types. Only solid-state and gas lasers are presently used in metalworking [5]. For higher continuous power outputs (> 1 kw), the CO_2 gas laser with an electrical efficiency of 15% is presently the only possible candidate laser system. It has been the development of commercially viable and reliable CO_2 lasers that has led to the current interest in laser surface modification technology [6].

As mentioned earlier, parameters which define specific operational modes are the laser beam power density and the time during which the laser beam interacts with the material surface (dwell time). Figure 3 shows the spectrum of commercial and experimental laser beam surface modification techniques as a function of power density and interaction time [7].

1. Surface treatments involving surface melting

In laser alloying a shallow surface layer is melted while alloying elements are added. In this way a thin surface layer with a desired local composition or microstructure is produced. Typical applications of this technique involve wear or corrosion resistance. Laser cladding is similar to conventional hardfacing whereby a prepositioned material is fused to the substrate, thus forming a protective layer. Compared with many conventional heat sources, the laser offers better control of coating geometry and reduced dilution because of minimal substrate melting. A common surfacing material could be, for example, stellite and the coating thicknesses are typically 0.25 mm. Potential applications are for valve seats, turbine-blade interlocks, piston rings, aluminum alloy components and nuclear fuel element assemblies. Laser glazing is a process which utilizes high power densities and relatively short specimen interaction times in order to melt and solidify the substrate sufficiently rapidly to produce an extremely fine-grained microstructure with improved wear or corrosion resistance. This treatment may also be used to eliminate surface defects or improve the integrity (homogeneity and adhesion) of overlay coatings applied by electrochemical techniques. Applications here could include turbine blade improvements, superhard coatings, and high performance composition.

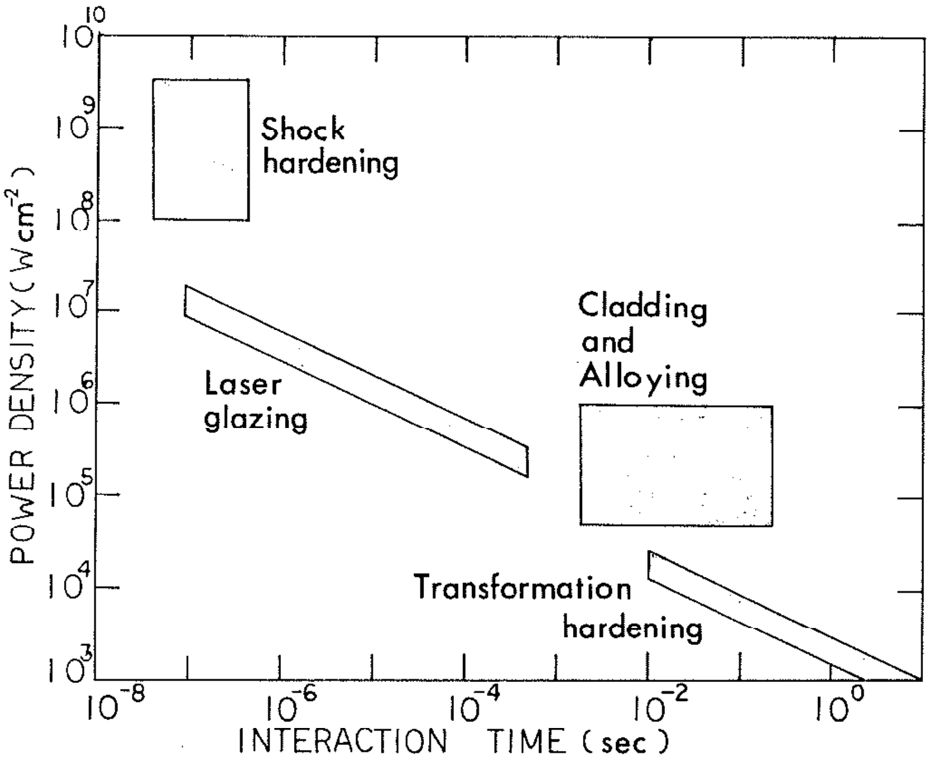

Figure 3. Operational regimes for the laser heat treatment of engineering materials [7].

Another process is shock hardening. This involves extremely high power densities and very short dwell time to work-harden materials with shock waves created by the vaporization of a sacrifical overlay. This treatment has been shown to be effective in improving fatigue life [7].

2. Surface treatments without melting

Tranformation hardening of ferrous alloys is a simple and very commercially active current metallurgical application of lasers. The same metallurgical principles underlie both conventional and laser hardening but, in the latter case, much shorter times are involved, with extremely high heating and cooling rates. Typically, laser hardening is employed where cases up to 1 mm thick are required, but deeper cases can be achieved by reducing beam power density and treatment rates. In transformation hardening a coating/coupling medium is necessary to increase the energy absorption by the metal specimen. Black paints, metal oxide powders, colloidal graphite and zinc/magnesium phosphates are suitable materials [7]. In a manner analogous to the effects of metallurgical variables in conventional heat treatment processes, alloy composition, pre-hardened microstructure and section thickness determine the final hardness and case depths attainable by laser hardening.

B. Wear and slurry erosion

1. Wear mechanisms

It is common to classify types of wear by using such terms as adhesive wear or rolling contact fatigue when well-defined wear mechanisms operate. An alternate classification scheme would be phenomenological. Simple descriptive terms such as sliding, rolling, impact, wet/dry, and lubricated/unlubricated wear are based on simple observations about the wear system, and they are more appropriate whenever the wear mechanisms are not unique or well characterized [8]. Two types of wear, sliding wear and abrasive wear, are the most common and of most importance in typical engineering applications. Other important wear processes include corrosive wear and surface fatigue wear [9]. In the following paragraphs detailed discussions of sliding wear and abrasive wear will be presented.

a. Sliding wear: The adhesion theory of wear recognizes that the real area of contact of two solids brought into close proximity is very small, the points of contact being only at the summits of the highest irregularities, asperites, in the surfaces. Consequently, the real area of contact is independent of the apparent area of the surfaces and is determined by the applied load. Under the high pressure at localized points of contact, elastic and plastic deformation occur until the areas of the contact junctions are large enough to support the load. The friction force required to cause sliding is in large measure the force required to shear these contact point junctions [10]. The volume of material removed during adhesive wear is described by the equation developed by Archard [11]:

$$V = K \cdot \frac{S}{3} \cdot \frac{L}{H} \quad ,$$

where V is the volume worn away, S is the sliding distance, L is the normal load, H is the indentation hardness value of the softer of the wearing pair, and K is a constant named the wear coefficient.

The adhesion theory involves the following sequence of events [10]:

(i) Flattening of asperites by deformation and the development of a high shear strength interface between the two surfaces.

(ii) Fracture in one of the materials at a position remote from the interface, removing a fragment from one material and transferring it to the other.

(iii) The detachment of the transferred fragment to become wear debris.

b. Abrasive wear: For abrasive wear by multi-particle contact there is a wide range of particle loadings, particle geometries and attack angles. Each of these factors has a considerable influence on both the mechanism of material removal and the wear rate. There are two extreme mechanisms of abrasive wear; one in which plastic deformation plays a predominant role and is the rate-controlling process, and the other in which fracture occurs with limited plastic deformation and is dominant and rate controlling [12].

Two major processes take place when abrasive particles contact the surface of a ductile material:

(i) The formation of grooves ("plowing") which do not involve direct material removal.

(ii) The separation of particles ("gouging") in the form of primary wear debris or microchips.

In both cases material is deformed to the sides of the grooves and can become detached to form secondary microchips. Ultimately, material is removed by fracture, but plastic deformation controls the rate at which the material is removed.

When a contacting abrasive particle forms a groove by plastic deformation we can represent the volume of material removed, ΔV, by:

$$\Delta V = K_1 \cdot K_2 \quad A \cdot \quad S$$

where K_1 is the probability that material is removed, K_2 is the proportion of the groove volume that forms wear debris, as opposed to that which is deformed to the sides of the groove, A is the cross-sectional area of the groove and S is the sliding distance.

During the indentation or scratching of brittle solids by a spherical indenter, fracture may occur under apparently elastic contact--Hertzian fracture--with the formation of conical cracks extending into the material. At small indenter radii of curvature elastic-plastic contact occurs because the radius of curvature has a larger effect on the plastic indentation load than on the Hertzian fracture load. For sharp indenters, the depth of elastic-plastic indentation increases with increasing load until the indentation reaches a critical size. At this critical size the tensile stresses are sufficient to cause cracks to propagate from the plastic zone surrounding the indentation. Material removal will occur when the lateral cracks intersect each other or propagate to the surface. When indentation fracture occurs, the crack lengths scale with the size of the indentation and are larger for material of low fracture toughness. Evans and Wilshaw [13] have modelled this process and predict that the upper limit for wear volume per unit sliding area per unit sliding distance is

$$W = N \cdot \bar{L}^{5/4} \cdot K_c^{-3/4} \cdot H^{-3/4} .$$

where N is the number of particles that contact the surface per unit area, $\bar{L}$, K_c, H are the mean load on the particle, fracture toughness and hardness of the surface, respectively.

2. Microstructure and abrasive wear resistance

Microstructural parameters such as inclusions, second phases, grain boundaries, matrix structure, internal notches and anisotropy are important to abrasive wear resistance [14].

a. Inclusions: Abrasive wear resistance of pure metals increases linearly with increasing hardness [15-16]. The wear resistance of steels, however, is less than that of pure metals of equal hardness because they contain inclusions which produce high local stress concentrations.

b. Second phases: Soft, coherent, intermetallic compound precipitates increase abrasive wear resistance only insignificantly compared with the super-saturated solid solution. The source of this unfavorable wear behavior of coherent particles is their low indentation hardness and the local work softening produced by shearing of the particles by dislocations. Non-shearable precipitates increase wear resistance in proportion to the hardness increment. The highest wear resistance is obtained in microstructures with fine, well dispersed semi-coherent particles [17]. Because of their hardness, carbides are particularly important for wear resistant materials. The influence of carbides on wear resistance depends on their hardness relative to matrix hardness. For carbides in a soft matrix, a small mean particle spacing, a small ratio of abrasive groove to carbide size, a high volume fraction of carbides, a high carbide hardness, and a low interface energy between carbide and matrix all favor high wear resistance [18,19]. For carbides in a hard matrix, if both have similar hardness, wear resistance suffers because the carbides act as internal notches.

Wear resistance of a material composed of both hard and soft phases generally decreases with increasing soft phase volume fraction because the soft phase is easily worn off. However, when the amount of retained austenite in a martensitic microstructure increases, hardness decreases but wear resistance increases. Under the high local deformation encountered in abrasive wear loading using a hard abrasive, some retained austenite can transform to martensite. Microhardness data also show that austenite hardness apprpoaches that of the surrounding martensite because of high work hardening. The austenite, however, is more ductile. In general, the loss of hardness attributed to retained austenite can be compensated for by an increase in work hardening rate.

c. Grain boundaries: Increasing hardness by grain refinement increases wear resistance. On the other hand, grain boundaries are frequently embrittled by segregation or precipitates, reducing the critical stress for grain boundary cracking. Under high abrasive loading, cracking can occur along prior grain boundaries and increase the wear rate.

d. Matrix structure: Wear resistance of ferrous alloys increases as microstructures are changed progressively from ferrite to pearlite, bainite, and finally martensite due to the increasing hardnesses. Abrasive wear resistance of a nodular ductile cast iron with different matrices is plotted as a function of matrix microhardness in figure 4 [20]. Because of their high hardness, the martensite and tempered martensite matrices have the highest wear resistance. At equal hardness, however, bainitic microstructures are much better than tempered martensite. Retained austenite is desirable in bainite structures because there is less difference between the hardness of bainite and austenite than there is between the hardness of martensite and austenite. After work hardening or transformation of the retained austenite, matrix hardness can be higher than that of a completely bainitic structure.

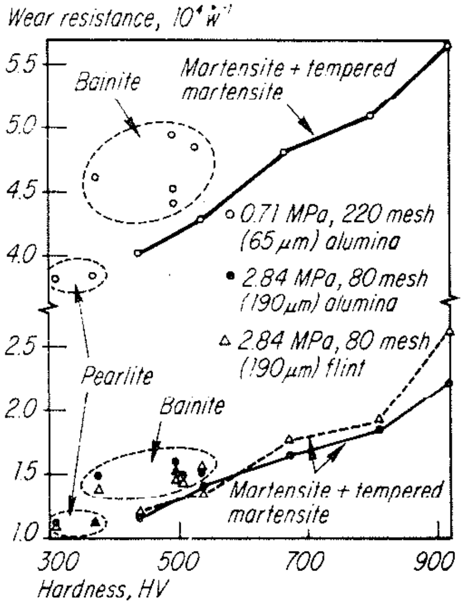

Figure 4. Influence of matrix microstructure on the wear resistance of ductile iron (3.33C, 2.26Si, 0.31Mn, 0.72Ni, 1.01Cu, 0.08Mg) [14].

Under conditions of identical load and grit size, the martensite resists abrasion by flint (~ 950 HV) much better than it does by alumina (~ 1800 HV).

e. Internal notches: Microcracks, pores, large carbides or inclusions, and lamellar or spherical graphite decrease wear resistance because they act as internal notches.

f. Anisotropy: Mechanical properties and wear rate depend on the loading direction because of both crystalline and structural anisotropy. Crystalline anisotropy has a very strong effect in hexagonal structures. Structural anisotropy can occur in aligned fibrous composites, or as a result of unidirectional solidification or precipitation of a second phase in a magnetic or stress field.

3. Slurry erosion

There is much literature on the erosion of metals by aqueous slurries. Test devices include loops [21-23] and slurry pot systems [24-26]. Test loops are attractive because they include components such as pumps, valves, bends and piping which are important in processing systems. Although accelerated wear tests of duration up to 24 h can be conducted with radioactive inserts, tests more commonly require times of 1000 hours or more. Pot tests are conducted in a flask or a beaker in which a slurry is agitated with a stirring propeller. Test specimens may be the stirring propeller or a small flat metal specimen placed at a tangent to the rotating slurry. Slurry pot tests have been useful in studying erosion-corrosion by aqueous coal slurries and they correlate better than do loop tests with field performance of pipelines containing a coal-water slurry [27].

a. Slurry abrasion mechanisms: The abrasion or erosion of materials by fluid-borne particles is primarily caused by a combination of two basic mechanisms: deformation wear and cutting wear [28].

(i) Deformation wear, as illustrated in figure 5(a), is caused by the impact of solid particles some of which have sufficient kinetic energy to cause local stresses higher than the yield point. Repeated application of these stresses and the accumulated strains lead to surface breakdown of the wearing material (also called fracture wear by M.A. Moore and others [12]).

(ii) Cutting wear, as illustrated in figure 5(b), is caused by the oblique impact of solid particles, some of which have sufficient energy to shear the surface of the wearing material and gouge a fragment loose (also called plastic deformation mechanism by M.A. Moore).

It has been shown by J.G.A. Bitter [29] that the relative effectiveness of deformation and cutting wear depends on the impingement angle of the abrasive particle as well as the nature of the wearing material. Figures 6(a) and 6(b) illustrate the abrasive wear rate in relation to the impingement angle for a ductile and a hard material, respectively.

b. Effects of testing variables on the erosion

A.V. Levy and W. Tsai [27] have shown that in a slurry pot erosion

(i) As the particle concentration increases, the erosion rate increases.

(ii) As the rotational speed increases, the erosion rate increases.

(iii) As the particles change from coal to SiC, the erosion rate increases substantially due to the increases in hardness, angularity and density relative to coal.

(iv) As the particle water content increases, the erosion rate decreases.

(v) As the testing temperature increases from 25°C to 100°C, the erosion rate decreases.

C. Laser surface hardening of cast iron

Laser hardening of cast iron was first accomplished in 1971 at the General Motors Manufacturing Development Center using a 250-watt CO_2 laser

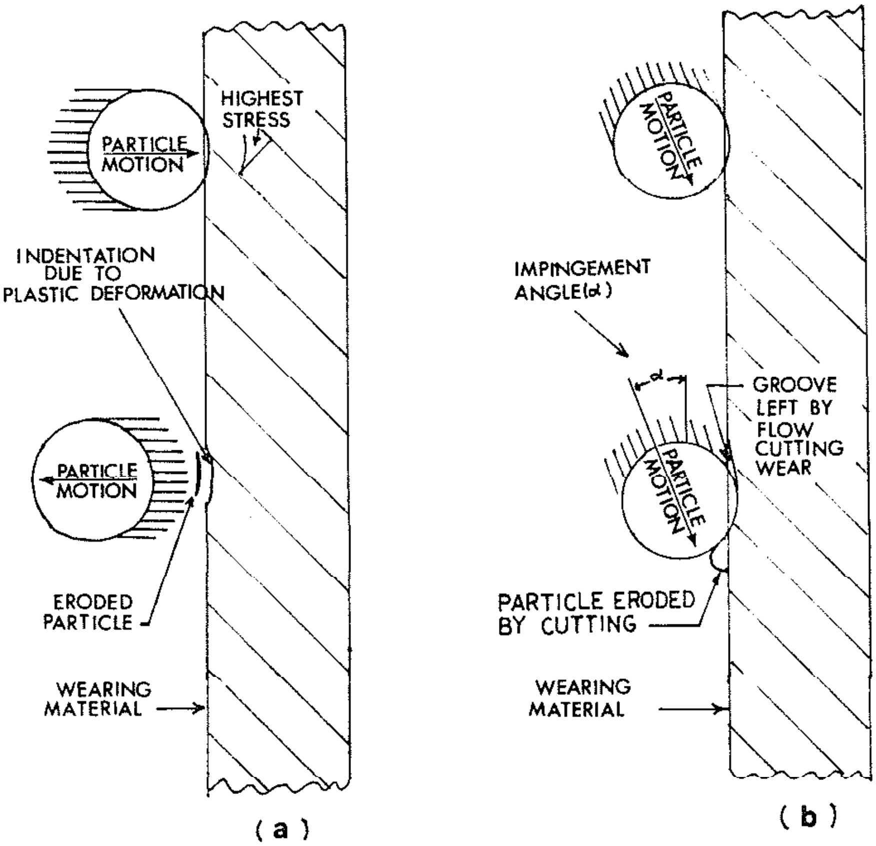

Figure 5. (a) Deformation abrasion
(b) Cutting abrasion [16].

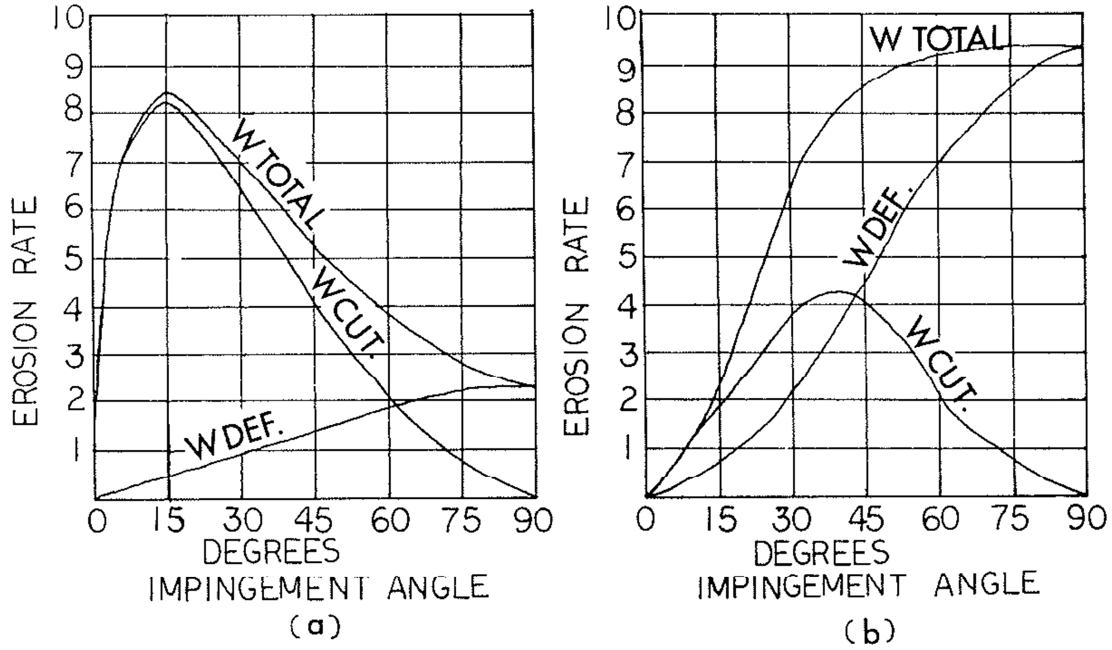

Figure 6. Erosion vs. impingement angle
(a) Ductile material
(b) Hardened material [17].

[30]. Since then, a variety of applications involving laser hardening of cast iron has been under development, primarily for the automobile industry. These applications are directed toward decreasing wear in metal-to-metal sliding or rotating contact. Examples are cast iron cylinder bores [31], valve guides, seal rings, camshafts [32], valve seals, gears and heavily loaded wearing surfaces.

In general, laser surface hardening of cast iron can be classified into 3 categories: transformation hardening, hardening with surface melting and rapid solidification with formation of an amorphous phase.

1. Transformation hardening: The transformation hardening process involves heating the material to below its melting point (but above the critical temperature for transformation) and allowing the essentially unheated bulk of the substrate to self-quench the heated surface layer to produce a martensitic matrix containing flake or nodular graphite with a measured hardness value of 57 to 60 HRC. It has been shown that 1550 to 2300 joules/cm^2 is suitable for transformation hardening gray cast iron, whereas 2300 to 3100 joules/cm^2 is required for alloying by surface melting [33]. By converting joules/cm^2 to dimensions applicable to the hardening job, one can determine the actual power per unit area required for a process. For example, with a laser beam spot size of 1 cm x 1 cm, a workpiece speed relative to the laser beam of 3 centimeters per second, and a six kilowatt incident beam power, the heating energy per unit area is 2000 joules/cm^2, which is in the suitable transformation hardening range.

$$\text{joules/cm}^2 = \text{watt-sec/cm}^2 = \frac{(\text{watt})(\text{length/scan speed})}{(\text{length})(\text{width})}$$

$$\frac{(6000\text{w})[(1\text{ cm})/(3\text{ cm/sec})]}{(1\text{ cm})\ (1\text{ cm})} = 2000\text{ joules/cm}^2 .$$

Various cast irons (nodular, malleable or gray) with a pearlitic matrix are readily transformation-hardened, because it is easy to produce the desired solution of carbon in the available time. Since the volume of material transformed is small, there is very little dimensional distortion and this hardening technique is widely accepted as a fully implemented production process.

2. Hardening with surface melting

a. ferritic malleable cast iron: The ferritic malleable cast iron matrix consists of widely spaced graphite nodules with very little dispersed carbide. Solid-state diffusion from the large graphite particles during laser processing would be too slow to produce the desired solution of carbon in the available time. Therefore, the power density of the laser beam is increased until melting occurs, because diffusion rates in the molten state are sufficiently rapid to produce a more uniform carbon dissolution and a hardened as-solidified surface layer. Using a CO_2 laser at a power of 1000 W and a scan speed of 50 mm/sec, a melted zone 0.3 mm deep and 2.0 mm wide can be achieved with a resulting hardness value around 57 HRC [31]. Ferrite melting at points of contact with graphite during laser hardening was reported in [34,35]. In the melted region one can distinguish two regions--a darker distinctly dendritic structure along the periphery and a lighter zone bordering the graphite. X-ray analysis showed that a high-carbon phase in the form of large dendrites of austenite is formed in the periphery in the direction of heat removal, while an austenite-cementite mixture is formed near the nucleus. The austenite, supersaturated with carbon, is unstable and may decompose [36].

b. High strength cast iron

A neodymium glass laser, generating 70 j pulses with a duration of 4 msec, was used to process high strength alloyed cast iron surfaces [37]. At the point of impingement there appeared a white layer with a thickness of 440 μm. The microhardness of the white layer is greater by more than a factor of two than the untreated cast iron. In the white layer, there is noted an increased content of carbon and chromium, while beneath the white layer there is a very slight decrease compared with the starting metal. The wear of cast iron with a white layer is less by a factor of three.

c. Synthetic cast iron with 3.0% C, 0.13% Al and traces of other elements: A neodymium glass laser, generating 100 j pulses with a duration of 1.8 msec, was used to process the cast iron surface [38]. In the surface layer, a finely dispersed assembly of long thin austenite dendrites in a cementite matrix was crystallized. The depth of fusion increased in the areas occupied by eutectic and secondary cementite, obviously because its melting point is low (1207°C according to Hillert [39]). The austenite dendrites are in the form of equiaxed sections through cylindrical crystals which grow perpendicular to the plane of the laser-melted surface layer.

d. Gray cast iron: Gray cast iron samples and parts were heated with a continuous CO_2 gas laser at 3 kW and beam speed of 0.5 m/min [40]. After laser treatment there were two distinct zones. In the first zone cooling occurred from the liquid and with increasing etching time one observed a series of pits oriented at an angle of 8-15° to the surface in the form of eutectic colonies of cementite. Near the central section of the zone of melting the crystallization of dendrites occurred in different directions, which is characteristic of primary cementite. At the boundary of the liquid and solid metal the dendrites were primarily perpendicular to the boundary, and the size of the dendrites was several times larger than in the central section. The hardness reached H_{50} 1000-1200 in the melted zone and did not depend on the speed of the beam or its power. At the boundary of liquid and solid metal porosity was observed, the spheroidal shape of the pores indicating that they were formed due to evolution of gases absorbed by graphite during crystallization of the cast iron. Phase analysis indicated that the zone of melting consisted of cementite, martensite, metastable austenite and ε phase. The wear of the laser treated gray cast iron was practically the same as that observed in high-alloy cast iron (18% Ni, 2% Cr, and 8% Cu).

3. Formation of amorphous phase

A pulsed neodymium glass laser with pulse energy of 100 j and a duration of 1.8 msec was used with the beam focused so that only a very shallow crater was formed on the surface of the cast iron [41]. The amorphous condition was obtained in chilled cast iron (3.20% C, 2.67% Si, 0.64% Mn, 0.014 % S, 0.060% P). In the zone of melting there were sections etched with nital along with nonetching sections. The well etched section consisted of a finely dispersed mixture of cementite and austenite, while the nonetching section was amorphous metal, i.e. "glass" not undergoing crystallization during rapid cooling at rates of $\sim 10^5 - 10^6$ K/sec due to the substantially higher concentration of dissolved carbon in the metal (~ 6%). Electron microscopic analysis showed that there were no signs of crystalline structure in this phase. The nonetching sections had a micro-hardness (under a load of 0.2 N) of H 1200 [41].

III. EXPERIMENTAL PROCEDURE

A. Material selection

Samples of pearlitic gray iron and ductile nodular iron with a pearlite/ferrite matrix were chosen because of their common usage in industry. These materials were donated courtesy of the Caterpillar Tractor Company. The ladle chemical analyses are shown in Table 1. The alloys were sand cast from 590 kg induction furnace heats and had the form of 5 cm x 10 cm x 60 cm bars. From these bars specimens were machined to 2.22 cm x 3.18 cm x 0.25 cm coupons and ground to a finish of 0.5 μm.

B. Laser treatment

1. Laser: The laser used is an AVCO EVERETT 10 kW CO_2 continuous wave laser located in the Materials Engineering Research Laboratory. The annular (TEM_{01}^{*}) laser beam can be focused using water cooled copper mirrors to a minimum diameter of approximately 0.1 cm, with a typical power level of 4 kW, producing a power density of approximately 500 kW/cm^2. A different output mode is possible using a beam integrating mirror which averages the power over a 1.25 cm square area. In this beam integrating mode much lower power densities are obtained.

2. Laser treatment: Because metals are highly reflective [2] at the 10.6 μm laser light wave length, the surface of each sample was coated with graphite to enhance absorption and assist in initiating melting. They were then laser melted and self quenched using the 10 kW CO_2 laser and a specially designed laser processing chamber which will be referred to as "LAMP" [42]. "LAMP" is a controlled environment chamber into which the laser beam energy is

Table 1

Chemical Analyses (wt.%)

elements cast irons	C	Si	S	P	Mn	Cr	Mo	Ni	Cu	Ti	Mg
gray	3.36	2.00	0.068	0.022	0.76	0.20	0.17	0.21	0.22	0.011	---
nodular	3.56	2.75	0.013	---	0.51	0.052	0.005	0.090	0.39	0.029	0.048

introduced through an infra-red transparent NaCl single crystal window and focused onto the sample surface (figure 7). The samples are mounted on the periphery of a water cooled copper wheel. Since the beam is stationary, the sample-holding wheel is connected to a variable speed drive motor that rotates it, thus giving the sample the effect of a scanning beam. In addition to rotation, another drive motor translates the wheel under the beam, hence, areas of significant size can be processed. The overlapping of individual melt stripes are produced by combination of the high rotational speed (up to 75 cm/sec) and the low translational speed (from 0.25 cm/min to 0.8 cm/min). He gas was blown onto the sample surfaces during laser processing to suppress plasma formation. The laser power levels used in this experiment ranged from 1/2 kW to 6 kW. The rotational speeds ranged from 2 RPM (1.67 cm/sec) to 50 RPM (41.7 cm/sec) and the translational speeds ranged from 0.06 cm/min to 0.8 cm/min.

In the integrated beam laser process, "LAMP" was not used. Samples were put directly on top of a controlled speed table equipped with x, y, z motion. He gas was blown directly onto the sample surfaces during processing to suppress plasma formation. The sample speeds relative to the beam ranged from 0.42 cm/sec to 2.08 cm/sec. The laser power levels used in this experiment ranged from 1.5 kW to 7 kW.

C. Erosion Tests

The erosion resistance of processed and unprocessed samples was tested using a water slurry abrasive system.

1. Slurry erosion tests: In order to determine erosion resistance in an abrasive slurry environment, a test unit was designed which was capable of:

a. simulating conditions of practical interests and also yielding meaningful and reproducible data.

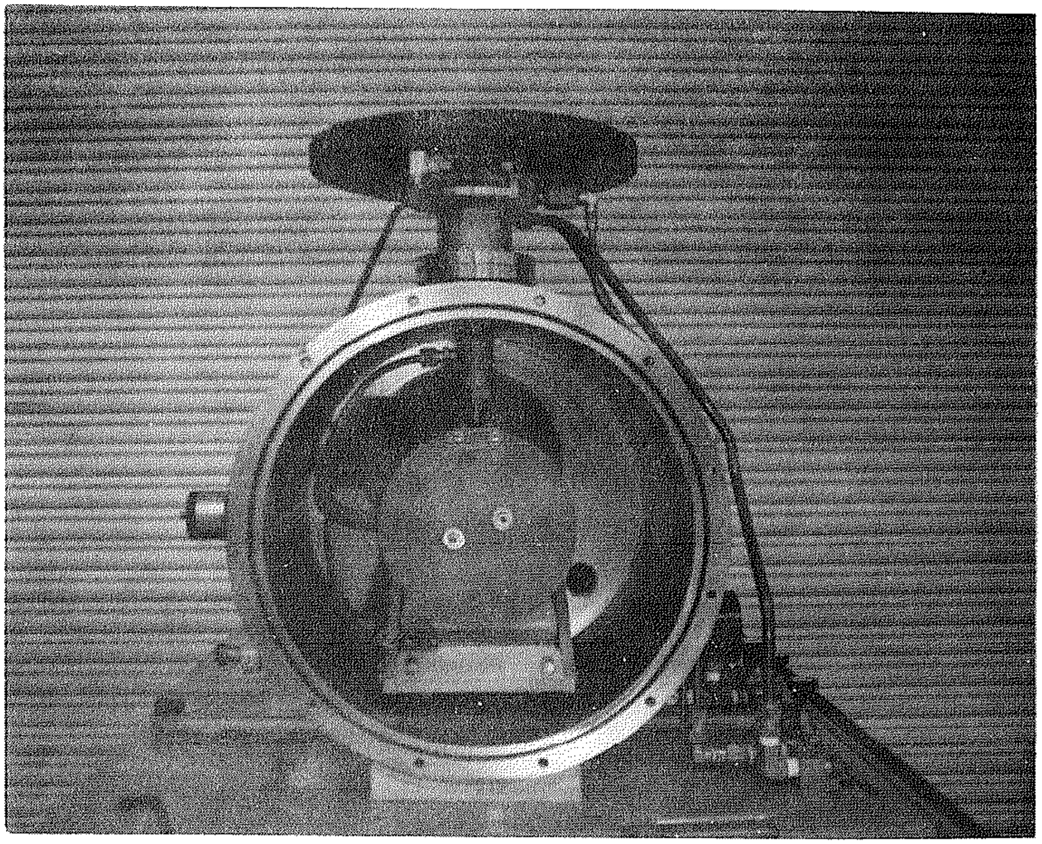

Figure 7. Front view of "LAMP" system with front cover plate removed to expose sample holder.

b. completing a test in a reasonable time at low cost.

c. obtaining results with a conveniently small amount of slurry.

d. maintaining a range of practical slurries in a uniform suspension without contamination during the test.

e. differentiating between specimens having different treatments.

In this work, accelerated erosion conditions were attained in the slurry erosion tester shown in figure 8. The tester consists of an erosion resistant enamel coated cylindrical tank with a cover. A slurry of SiO_2 or SiC particles in 2.3 kg of water was contained in the tank. It was fluidized by rotating the samples in a manner such that they serve as propeller blades (figure 9). The four sample holders were attached to a stainless steel shaft aligned along the axis of cylindrical symmetry, and the angles were adjusted to 45° to the rotation axis. Four samples, each of dimension 2.22 cm x 3.81 cm x 0.25 cm were mounted on the sample holders separately and secured in place by a set screw at the edge. The shaft was made to rotate at a controlled speed by a 1/4 HP motor equipped with a variable torque-speed regulator. A 60-tooth encoder mounted on the shaft above the motor allowed measurement of shaft rotation speed (to ± 1 RPM count) by means of a magnetic pick-up connected to a digital counter. Four TEFLON baffles attached to the inside wall of the cylinder ensured good mixing of the slurry by opposing the rotational and vortical motion induced by the rotating sample holder assembly.

2. Slurry erosion tests: Before testing, the samples were washed with acetone, dried and weighed with an accuracy of ± 0.1 mg. Then the perimeters of the sample surfaces were coated with thick thermosetting plastic, leaving a 2 cm x 1.5 cm exposed area in the center. Erosion depth was correlated with weight loss measurements and surface profiles were determined from both masked and unmasked areas.

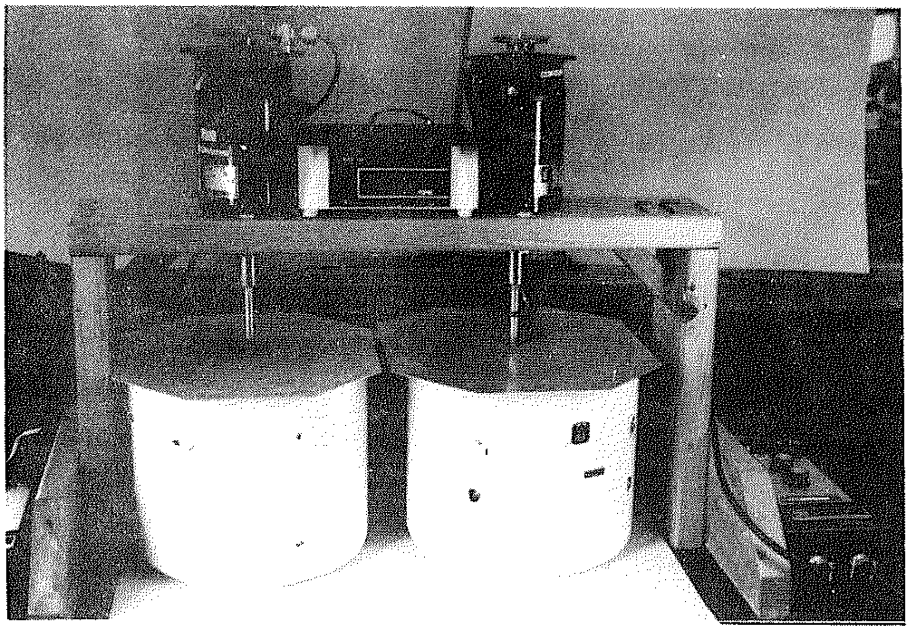

Figure 8. Slurry erosion tester.

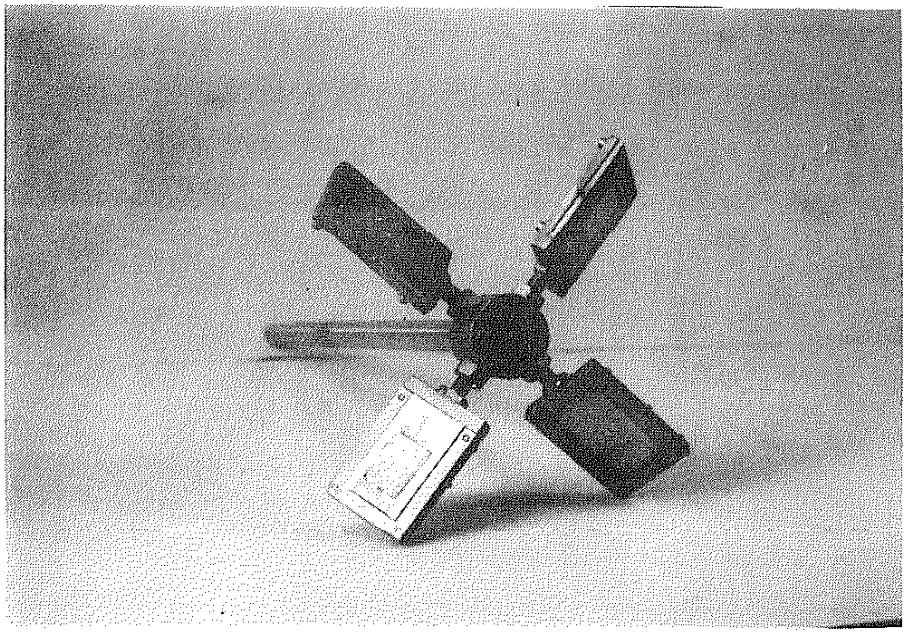

Figure 9. Sample holder assembly.

Initially, fine particle size SiO_2 (~ 45 μm) and SiC (~ 60 μm) abrasives were used to make slurries as thick as 66 wt.%. These slurries produced very low erosion rates and would require prohibitively long testing times. This problem was solved by switching to larger particle size SiO_2 and SiC abrasives. AFS 50/70 mesh SiO_2 of average particle size 250 μm (figure 10) was then used to make a 35 wt.% (17 vol %) water slurry. The rotating speed was set at 575 RPM with the sample surfaces positioned at a 45° angle face down. The testing was done in 2 to 6 hour increments. Surfaces of both unprocessed and processed (with a variety of laser processing conditions) samples were tested. After testing, the protective coatings were peeled off, the samples were cleaned in acetone, dried and weighed to get the weight loss. A surface profilometer was also used to measure the erosion depths and the surface roughnesses. These were related to the weight loss. The testing cycle was then repeated with total testing times as long as 112 hours. SiC particles of the same size range as the SiO_2 (figure 11) were also used to make a 35 wt.% (14.5 vol %) slurry to compare the erosion effects of different erosion particles.

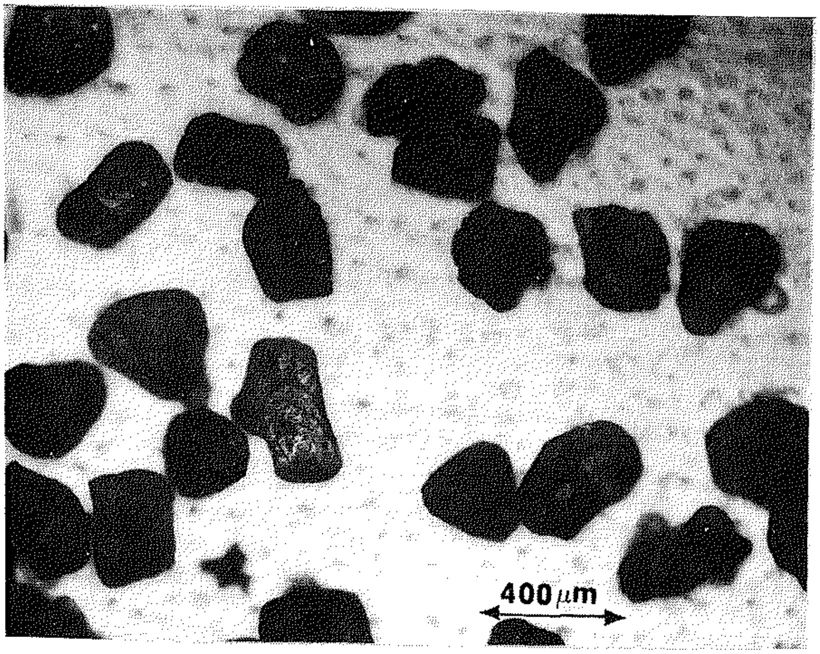

Figure 10. AFS 50/70 SiO_2 (~ 250 μm) testing sand. 50x

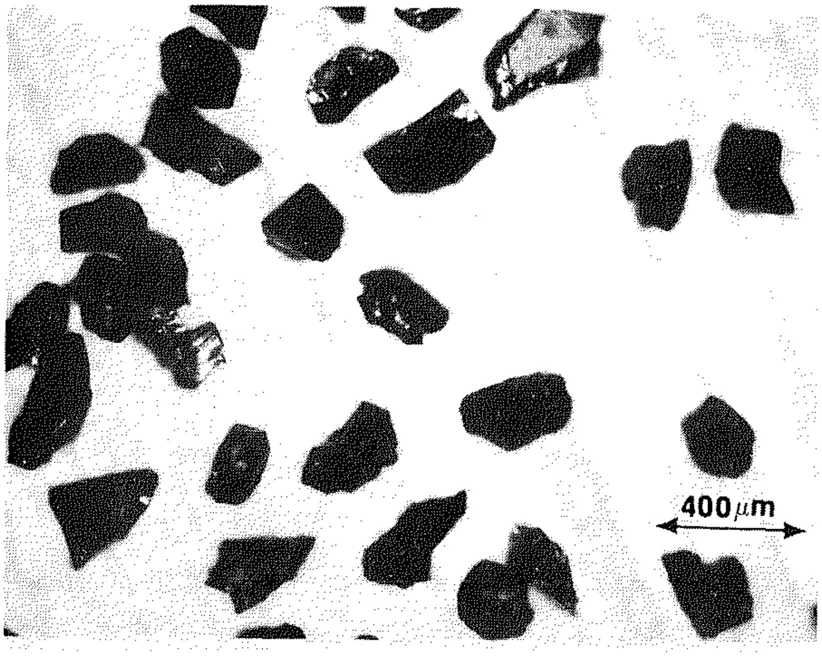

Figure 11. SiC (~ 250 μm) abrasive. 50x

IV. RESULTS

A. Laser surface processing

1. Starting material: microstructure and hardness

Figures 12 and 13 show the as-received microstructure of ductile cast iron and gray cast iron respectively. Ductile cast iron before laser treatment had an average hardness of HRB 98, while gray cast iron averaged HRB 90. The microstructure of ductile cast iron consisted of a pearlite matrix with graphite nodules and ferrite surrounding the graphite. The microstructure of gray cast iron consinsted of a pearlite matrix and graphite flakes.

2. High power density (focussed beam) laser processing:

Cast iron specimens were mounted on a water-cooled copper wheel and processed by rotation and translation beneath the laser beam. Surface microstructure modification was controlled by changing the rotational and translational speeds and the laser power (1/2 kW to 6 kW). Gray cast iron and ductile cast iron samples laser processed by this technique are shown in figure 14. Both samples were processed at 4 kW, 25 RPM rotational speed (20.8 cm/sec linear speed), and 0.76 cm/min translational speed. The depths and hardnesses of the laser hardened layers for different processing conditions are shown in Table 2. After processing with the focussed beam, cast iron can reach a hardness as high as DPH 1245, with a hardened layer as deep as 1 mm. Processing conditions of slower scan speed and higher power input tended to result in deeper hardened layers and higher corresponding hardnesses. In the case of gray iron at 1 to 4 kW, both 10 RPM and 2 RPM yielded a high hardness (DPH 945 to 1245), while in ductile iron, only at 2

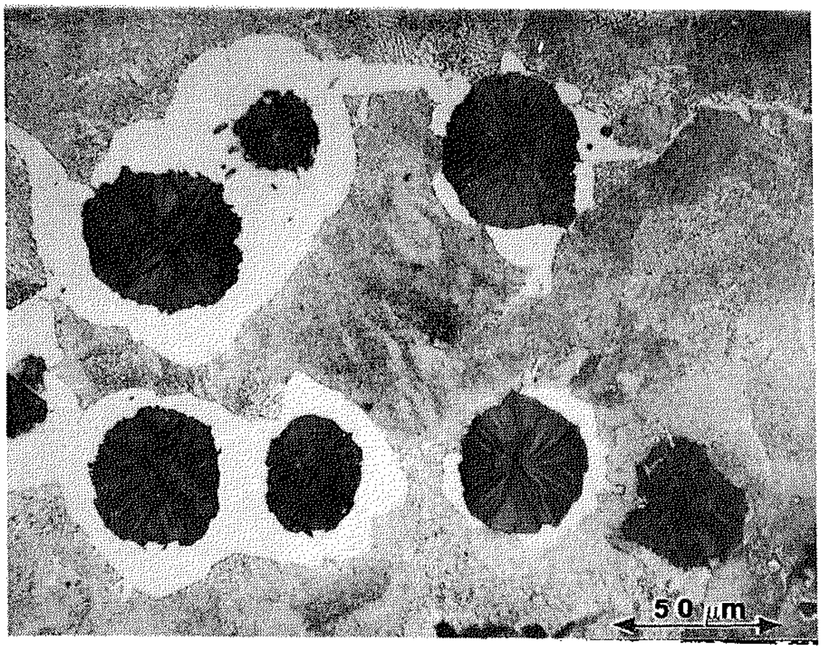

Figure 12. Microstructure of as-received ductile cast iron 400x (etchant = 4% picral).

Figure 13. Microstructure of as-received gray cast iron 400x (etchant = 4% picral).

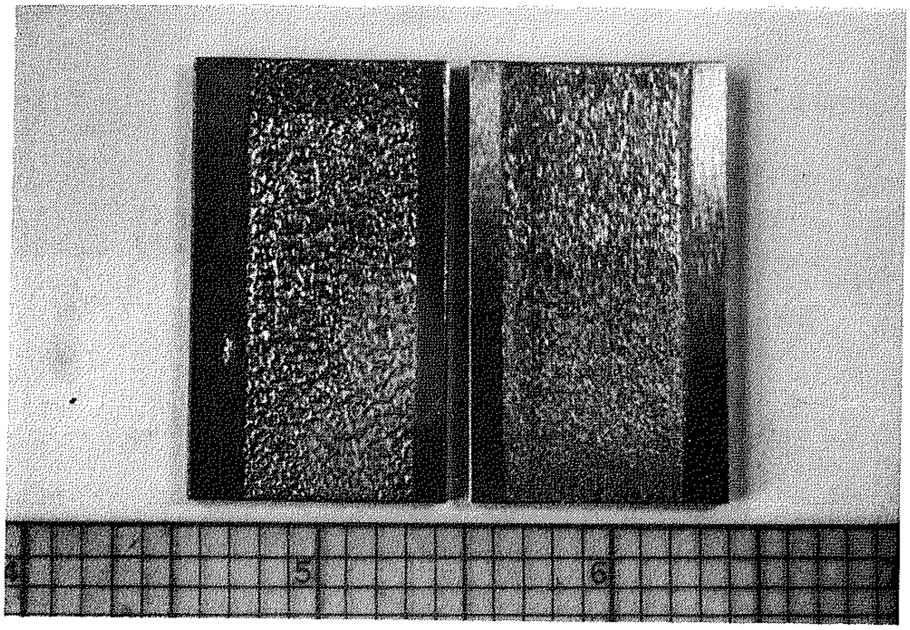

Figure 14. Laser processed surfaces of gray cast iron (left, has been shot blasted to reveal small pin-holes after laser treatment) and ductile iron (right). Both samples were processed at 4 kW, 25 RPM rotation speed (20.8 cm/sec sample linear speed), and 0.75 cm/min translational speed.

Table 2

Hardnesses and Hardened Layer Depths of Focussed Beam Laser Processed Cast Irons

Laser Variables		microhardness (DPH)		Average Depth of layer (mm)	
Power level (kW)	rotational* speed (RPM)	ductile	gray	ductile	gray
1/2	10	580	562	0.05	0.05
	2	725	716	0.18	0.20
1	25	---	560	---	0.05
	15	---	720	---	0.15
	10 Δ	600	945 o	0.10	0.15
	5	665	---	0.20	---
	2 Δ	1160 o	1160 o	0.30	0.30
2	23	617	655	0.05	0.10
	10 Δ	636	1076 o	0.20	0.20
	5	894	840	0.25	0.30
	2 Δ	1245 o	1162 o	0.50	0.50
3	25	655	---	0.10	---
4	25	660	700	0.15	0.25
	15	675	820	0.20	0.20
	10 Δ	725	1100 o	0.30	0.30
	5	945 o	940	0.80	0.90
	2 Δ	1245 o	1162 o	0.80	1.00

* The translational speeds were adjusted relative to each rotational speed to obtain 3 overlaps on each spot.
1 RPM = a velocity of 0.83 cm/sec of the specimen relative to the laser beam.

Δ Full amount of cooling water beneath the specimens.

o Feathery microstruocture, while all the others are dendritic.

RPM and 4 kW 5 RPM was this achieved. These high hardness layers had a fine feathery microstructure, while the other, lower hardness layers had a fine dendritic microstructure.

The microhardness of laser processed gray and ductile cast iron is shown in figure 15 as a function of distance from the laser processed surface. At the same processing condition (4 kW 10 RPM), the gray iron with a feathery microstructure (DPH 1100) was much harder than the ductile iron with a dendritic microstructure (DPH 725). At as faster speed (15 RPm, 25 RPM), both gray and ductile irons showed decreased hardnesses. A sudden drop in hardness at the mid-depth of the hardened layers corresponded to the overlapping of the laser beam on successive passes over the specimen. All the surfaces of the hardened layers showed slightly lower hardnesses than the average values.

In general, gray cast iron always had a rougher surface than ductile cast iron after laser processing. Figure 16 shows the surface profiles of laser processed gray cast iron for several processing conditions. At a high sample speed (25 RPM), both 1 kW and 4 kW processing resulted in a very rough surface. As the speed decreased the surface became smoother, however, at a slow speed of 5 RPM, the surface was melted so extensively that there was a hump along with a depression on it.

Figures 17 and 18 show the surface appearance of laser processed gray and ductile cast irons for various laser processing conditions at a magnification of 7x, and it can be seen again that gray iron had a much rougher surface than ductile iron after laser processing. As the total energy input increased, i.e., higher power and slower sample rotational speed, the hardened depths of both cast irons increased and the surface became smoother. However, it is

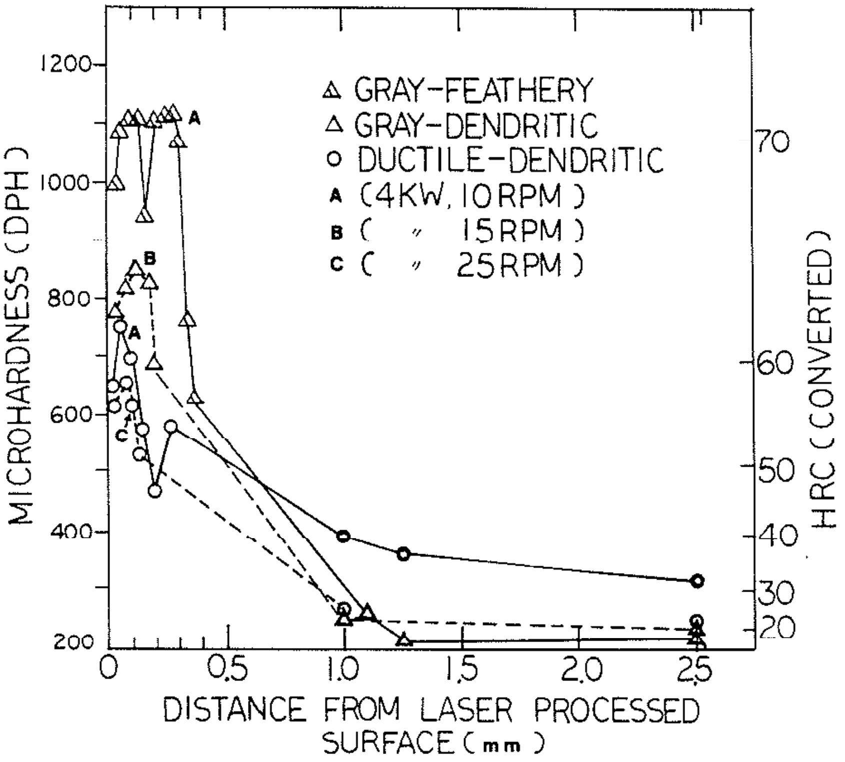

Figure 15. Microhardness of laser processed cast irons.

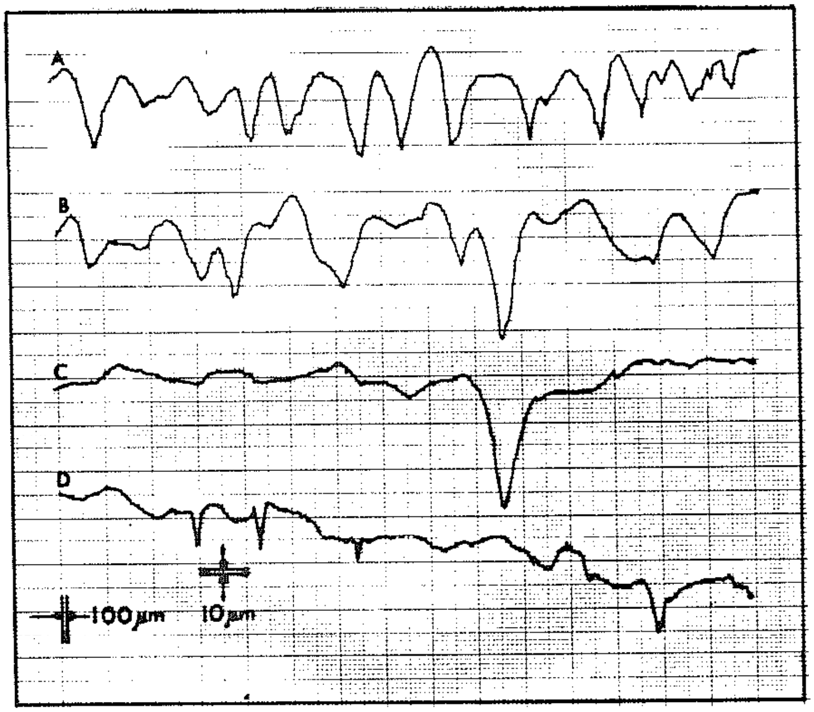

Figure 16. Surface profiles parallel to beam travel direction of laser processed gray cast iron.
A = 1 kW, 25 RPM; B = 4 kW, 25 RPM
C = 4 kW, 15 RPM; D = 4 kW, 5 RPM.

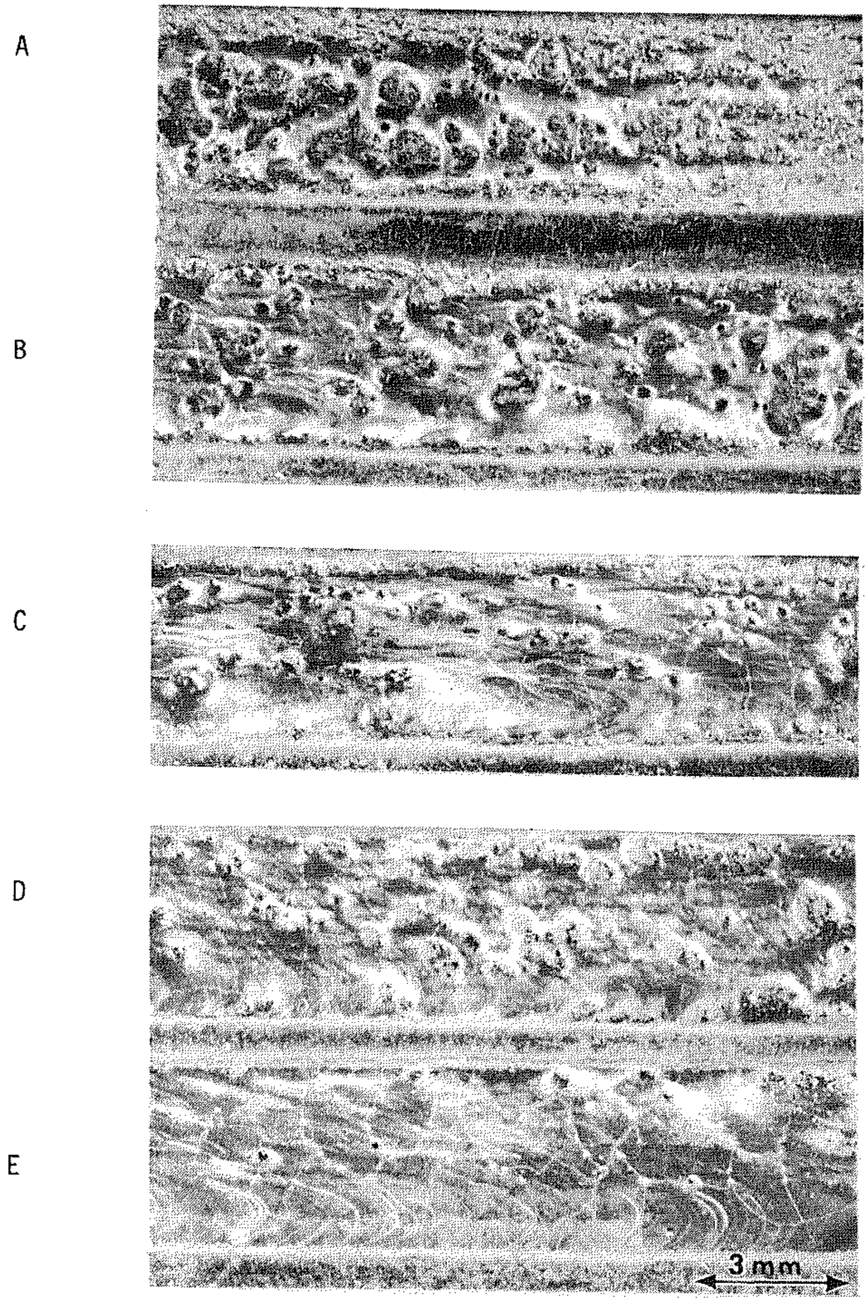

Figure 17. Surface appearances of laser processed gray iron. A = 1 kW, 10 RPM; B = 2 kW, 10 RPM; C = 4 kW, 10 RPM; D = 1 kW, 2 RPM; E = 2 kW, 2 RPM. 7x

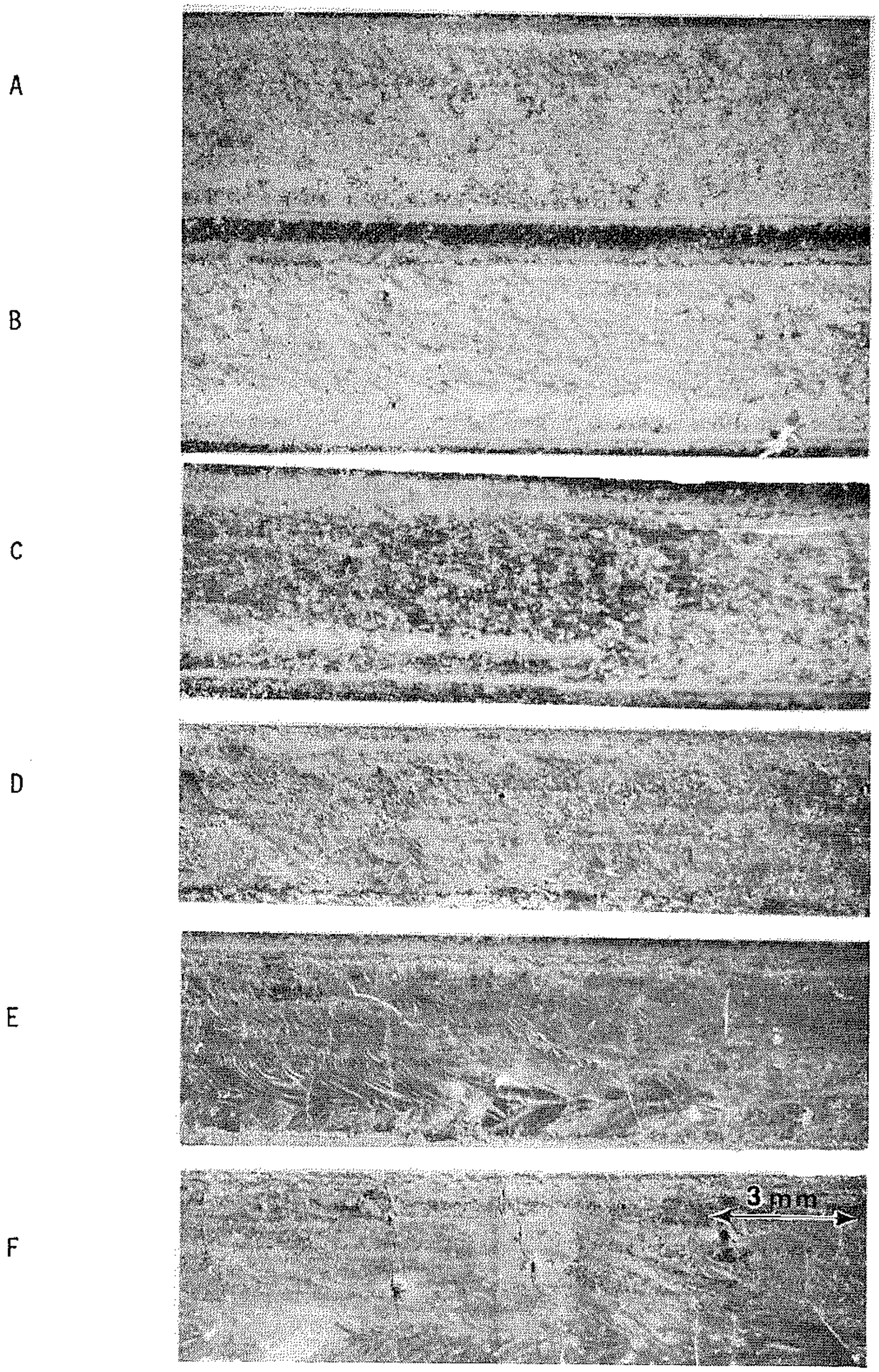

Figure 18. Surface appearance of laser processed ductile iron. A = 1 kW, 10 RPM; B = 2 kW, 10 RPM; C = 4 kW, 10 RPM; D = 1 kW, 2 RPM; E = 2 kW, 2 RPM; F = 4 kW, 2 RPM. 7x

also observed that increased heat input causes more visible transverse surface cracks. Figure 19 shows the surface appearance and cracks of gray cast iron after laser processing at 2 kW 2 RPM.

Figure 20 is a typical cross-sectional view of gray iron after laser processing. The hardened layer can easily be distinguished from the original gray iron matrix as the light region. The darker etching bands in the processed layer are the results of heating produced by the overlapping of laser passes. At the boundary, the graphite flakes are observed to be only partly dissolved in the hardened layer. There was a very thin heat affected zone beneath the hardened layer, ranging from 5 to 40 μm in depth. At 4 kW and 5 RPM or 2 RPM, the surface was melted so extensively that there was a macroscopic flow of liquid along the specimen surface in a direction opposite to the rotational movement of the specimen mounting wheel. The resulting surface consequently had a hump at one end and a depression at the other end. The best processing conditions combining good depth with a smooth surface and minimum surface cracking were found to be 4 kW, 25 RPM for ductile cast iron and 4 kW, 15 RPM for gray cast iron.

After laser processing there are basically two kinds of microstructures, as shown in Figures 21, 22, 23 and 24. Figure 21 shows a ductile iron laser processed at 4 kW 25 RPM, with a dendritic microstructure and an average hardness of DPH 660. Figure 22 shows a ductile iron laser processed at 4 kW 2 RPM, with a feathery microstructure and an average hardness of DPH 1245. Figure 23 shows a gray iron processed at 4 kW 15 RPM with a dendritic microstructure and an average hardness of DPH 820. Figure 24 shows a gray iron processed at 4 kW 2 RPM with a feathery microstructure and an average hardness of DPH 1162. The feathery microstructure has a higher hardness (DPH 945 to

Figure 19. Surface appearance and cracks of laser processed gray iron (2 kW, 2 RPM, 3 overlaps). 50x

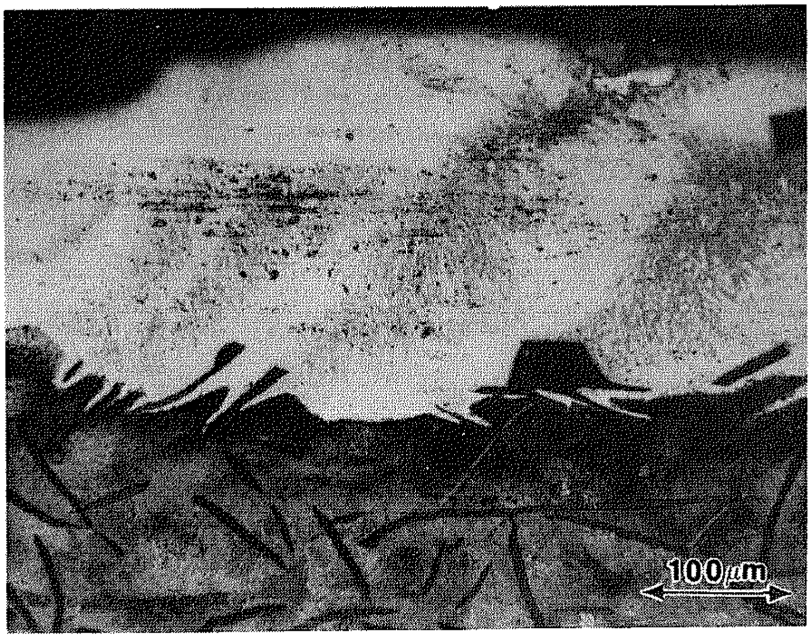

Figure 20. Sectional view of laser processed gray iron (2 kW, 5 RPM) 200x, etchant = 4% picral.

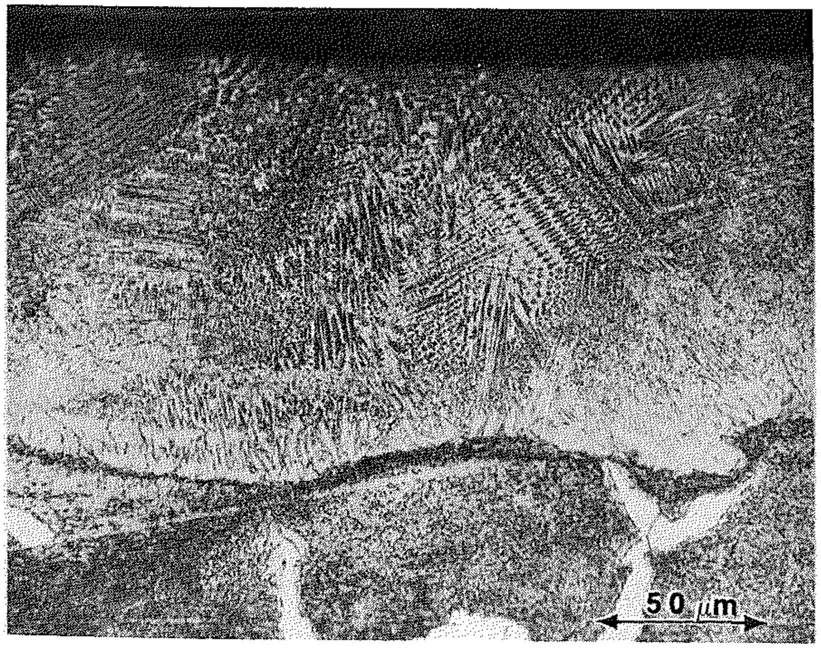

Figure 21. Laser processed ductile iron showing dendritic structure with an average hardness of DPH 660 (4 kW, 25 RPM). 400x

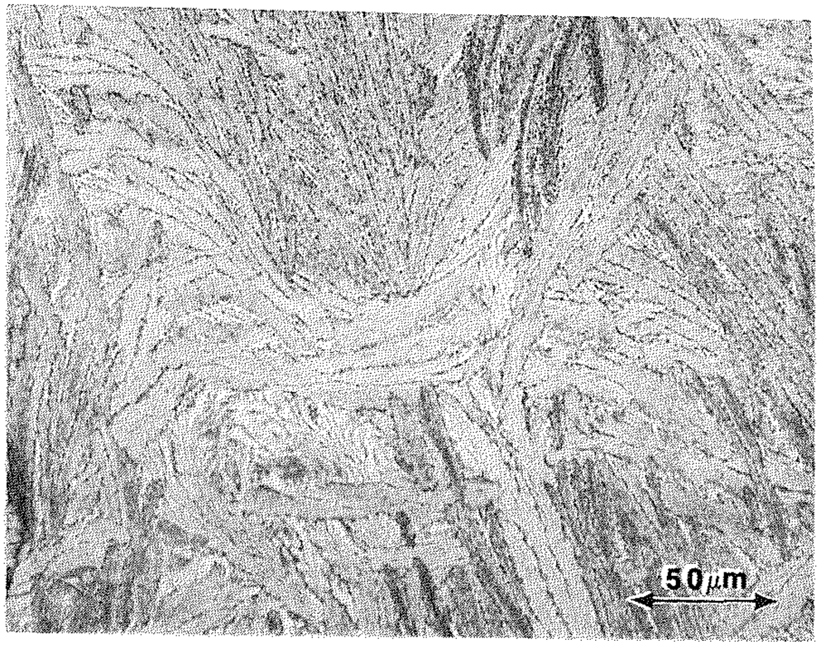

Figure 22. Laser processed ductile iron showing feathery structure with an average hardness of DPH 1245 (4 kW, 2 RPM). 400x.

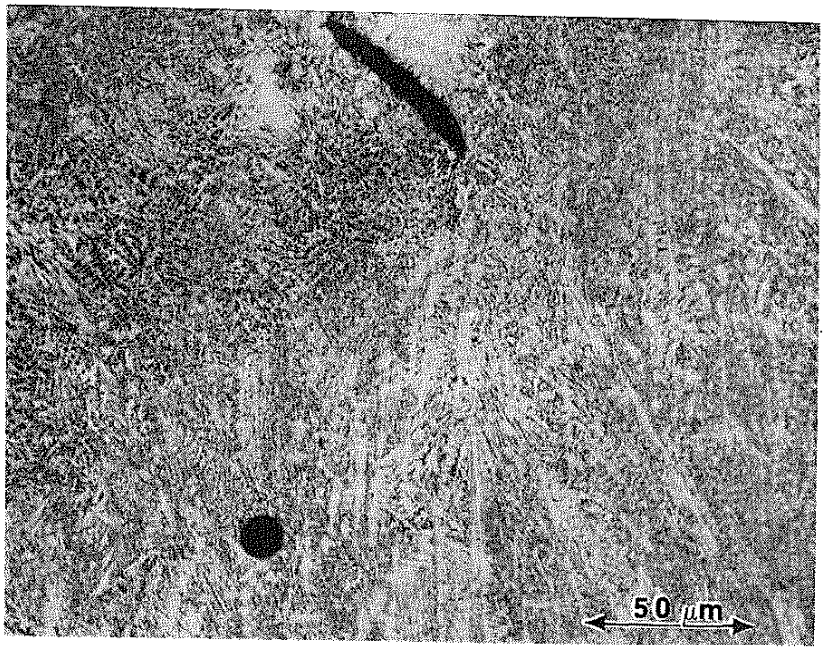

Figure 23. Laser processed gray iron showing dendritic structure with an average hardness of DPH 820 (4 kW, 15 RPM). 400x

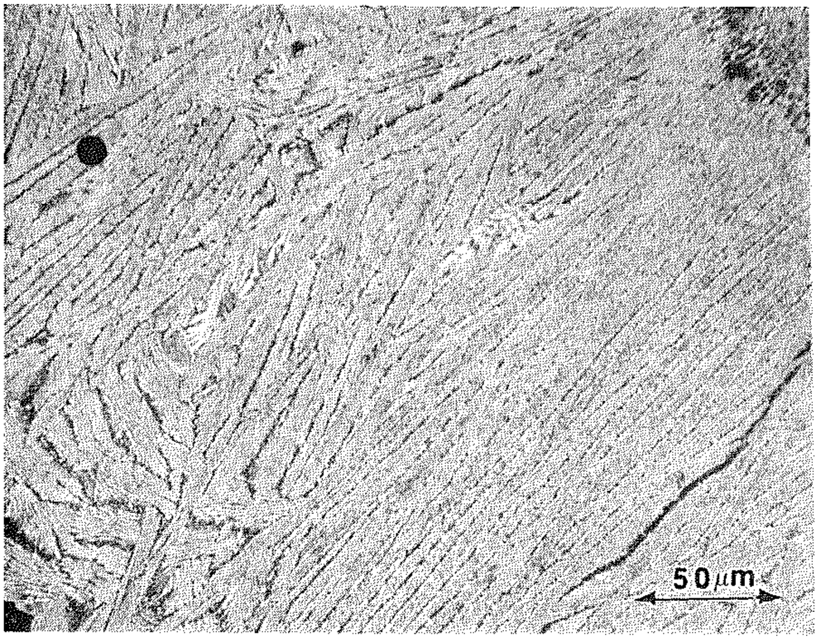

Figure 24. Laser processed gray iron showing feathery structure with an average hardness of DPH 1162 (4 kW, 2 RPM). 400x.

1245), while the hardnesses of dendritic microstructure ranges from DPH 560 to 940. However, there are problems which arise when the processing conditions result in the feathery structure. For example, more surface cracks are formed and, for too low a sample speed, the surface was severely distorted. For the gray iron, there were always some pores in the vicinity of the boundary between the hardened layer and the unmelted substrate.

SEM examination, figure 25, shows the dendritic structure of the surface of a ductile iron sample processed at 4 kW and 25 RPM. The average dendrite size is about 2 μm and the dendrite patches line up in the direction of sample motion.

The bright-field TEM micrograph, figure 26, shows the dendritic structure of the laser processed layer. The matrix consists of a single phase, with many dislocations in it. The interdendritic region may be some sort of carbide, and needs further investigation. Analysis of a selected area electron diffraction pattern of the matrix (dendrite) material (figure 26) showed that it is face centered cubic with $\{100\}$ planes parallel to the surface of the foil.

EDX-TEM microchemical analysis results on dendrite and interdendritic regions are shown in figure 27 and table 3. The dendrite was found to have a higher Si content while the interdendritic region had a higher Fe, Mn, Ti, Cr, and V content. The compositional analyses were done without standards and therefore should be considered qualitative. However, the relative composition differences between the two phases is correct. X-ray diffraction patterns from as-received and laser process (4 kW, 25 RPM) ductile iron are shown in figures 28 and 29, respectively. As-received ductile iron was found to have a ferritic matrix with evidence of a small retained austenite content.

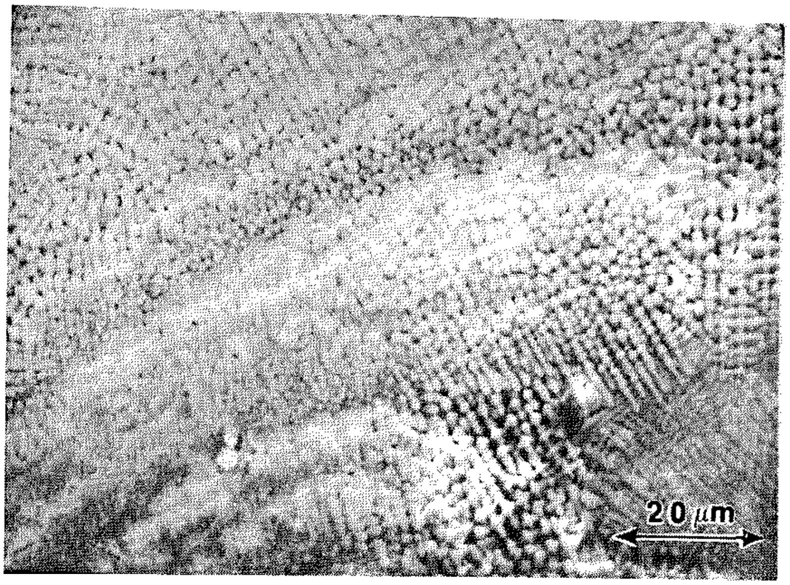

Figure 25. SEM surface feature of laser processed ductile iron (4 kW, 25 RPM). 1000x

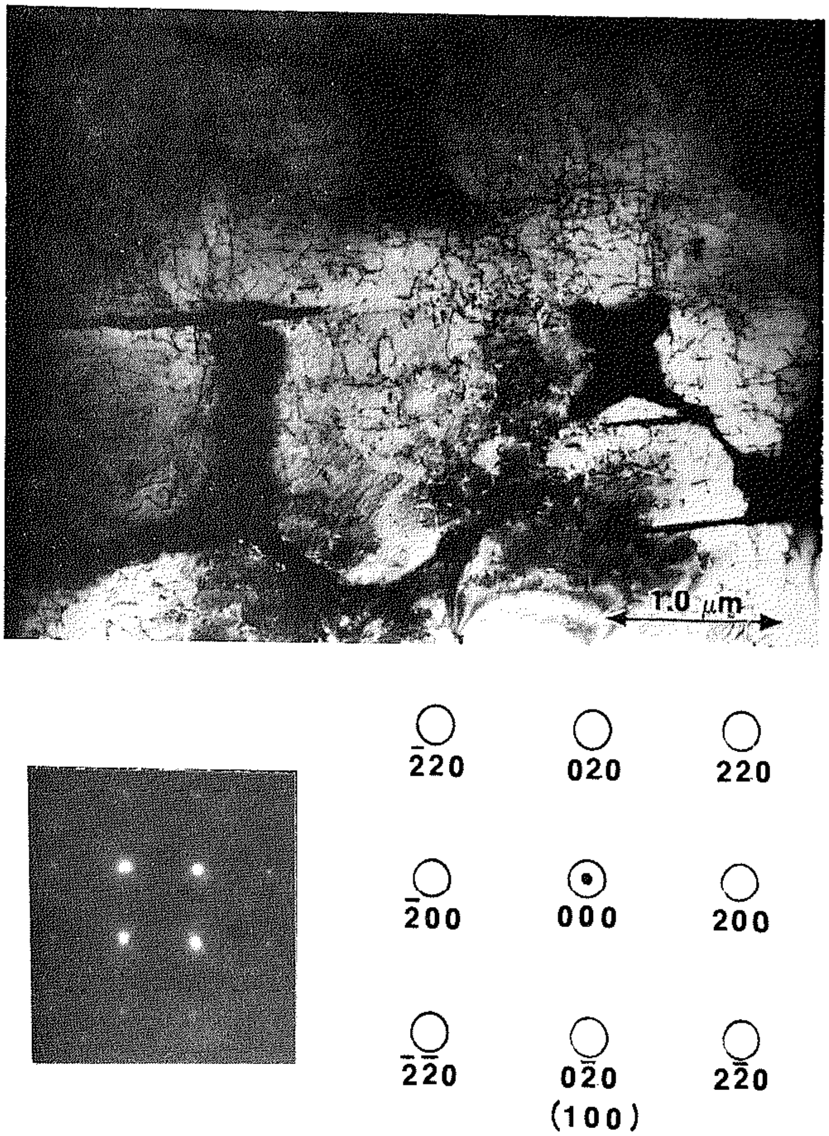

Figure 26. TEM bright field micrograph (20,000x) accompanied by a selected area diffraction pattern of a dendrite (ductile iron processed at 4 kW, 25 RPM).

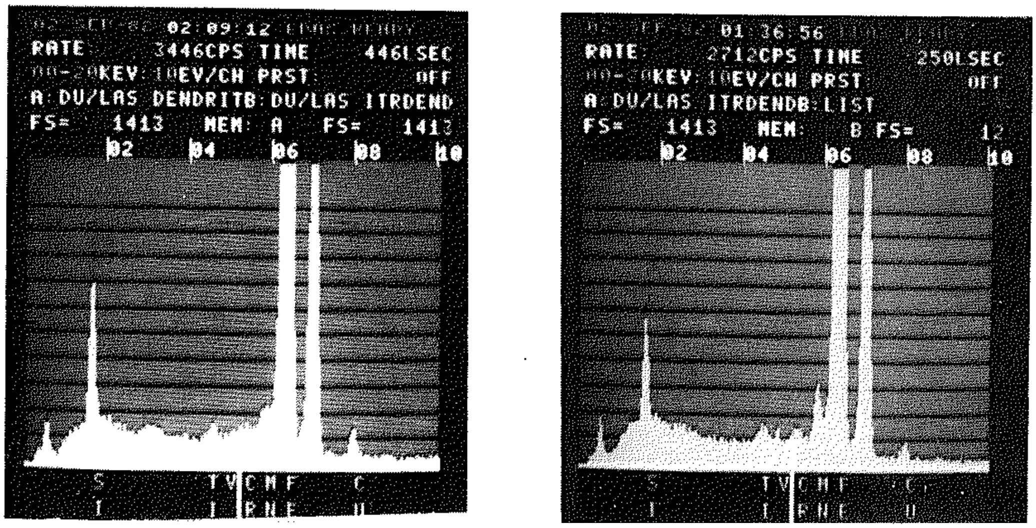

(a) (b)

Figure 27. EDX microchemical analyses of the (a) dendrite and (b) interdendritic region.

Table 3

Phase Compositions

Element wt.% / Phase	Fe	Si	Mn	Cu	Ti	Cr	V
dendrite	71.2	27.3	0.11	1.3	0.06	---	---
interdendritic regions	76.5	20.5	1.2	1.1	0.40	0.20	0.17

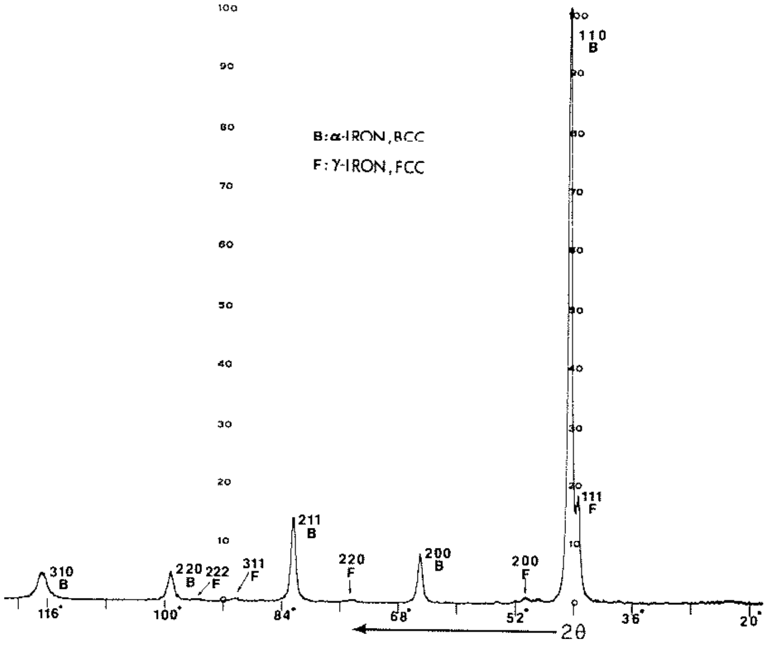

Figure 28. X-ray diffraction pattern of as-received ductile iron. Cu K_α radiation.

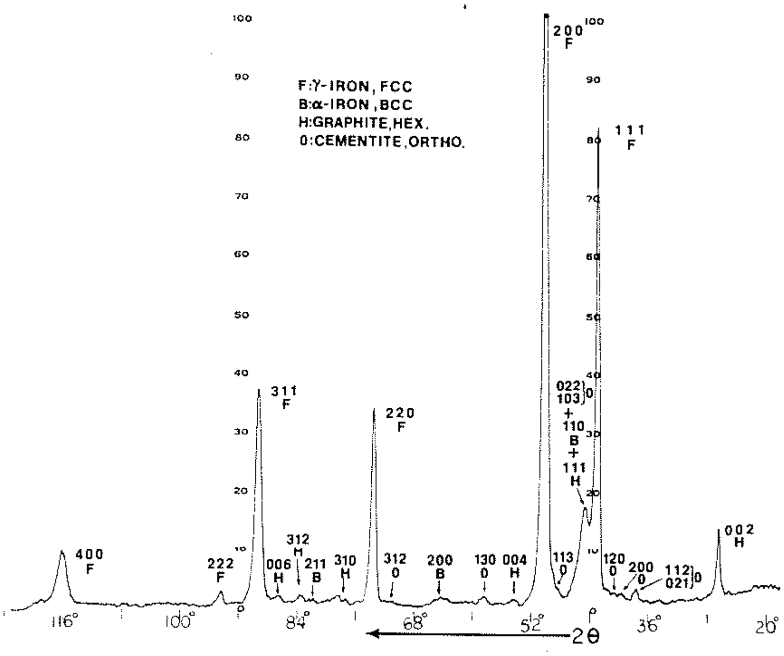

Figure 29. X-ray of laser processed (4 kW, 25 RPM) ductile iron. Cu K_α radiation.

The laser processed ductile iron was found to have an austenitic matrix with a small amount of graphite, ferrite and cementite. The face centered cubic dendrite matrix lattice parameter was found to have a value of 3.63 Å.

3. Integrating mirror laser processing

The power density with this processing mode is reduced by about 150 times relative to that of the focussed annular beam. This treatment produced a smoother surface without cracking and with an even deeper hardened depth than that obtained with the focussed annular beam. Hardness and hardened layer depth values for several processing conditions are shown in table 4. The hardness values of this laser processing are about the same as the values obtained by 4 kW 15 or 25 RPM focussed beam laser processing, however, the hardened layers are much deeper in the integrated beam case. Figures 30 to 33 show typical microstructures of low power density mirror laser processed gray iron (at 7 kW, 2.08 cm/sec sample speed). There are three kinds of microstructure: in the laser melted zone, it is basically white cast iron (see figure 31); in the laser overlap region, the matrix has the white cast iron structure with some dark, round phase scattered around (see figure 32); below the melted layer, the matrix is martensite in austenite with graphite remaining in flake shapes (figure 33).

Figures 34 to 37 show typical microstructures of low power density laser processed ductile iron. It also has three kinds of structures: the white cast iron structure (figure 36), the martensite-austenite structure (see figure 35), and in the overlap region, a bainite matrix with very fine and uniformly dispersed graphite particles (see figure 37).

Table 4

Hardness and Hardened Layer Depths of Integrated Beam Laser Processed Cast Irons

Laser variables		Microhardness (DPH)		Average depth of layer (mm)	
Power level (kW)	Specimen Transport rate cm/sec)	ductile	gray	ductile	gray
1.5	0.42	675	---	0.7*	---
2.5	0.83	650	---	0.65*	---
7.0	2.08	---	740 (636 in the overlapped area)	---	0.55

*Some graphite nodules floated to the surface during laser processing.

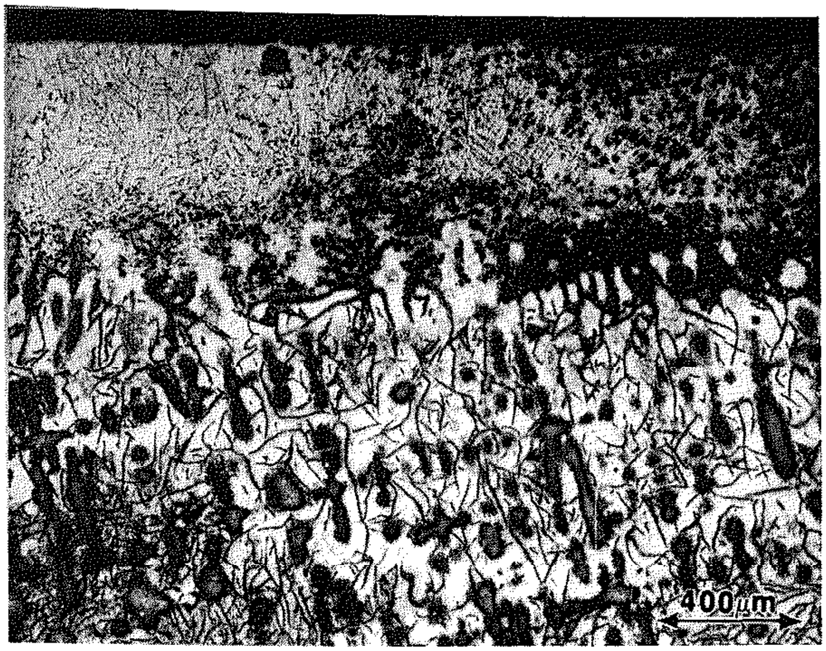

Figure 30. Microstructure of integrated beam laser processed gray iron (7 kW, 2.08 cm/sec). 50x

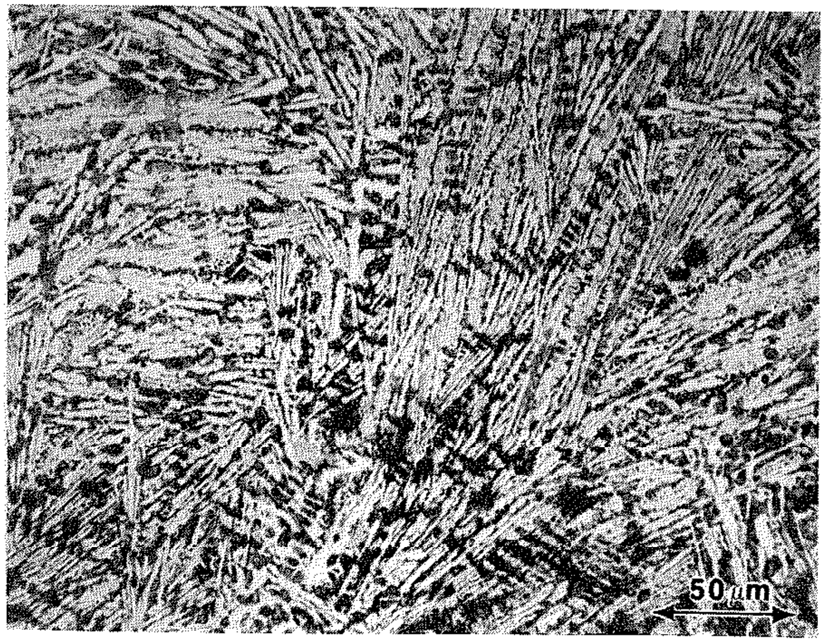

Figure 31. Same as above, upper left portion of figure 30. 400x.

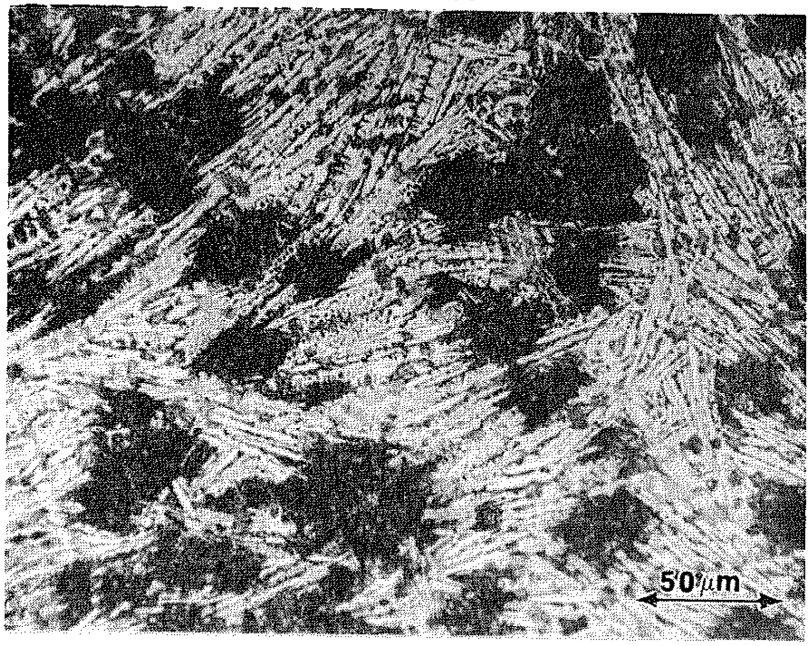

Figure 32. Upper right portion of figure 30 (laser path overlap area). 400x

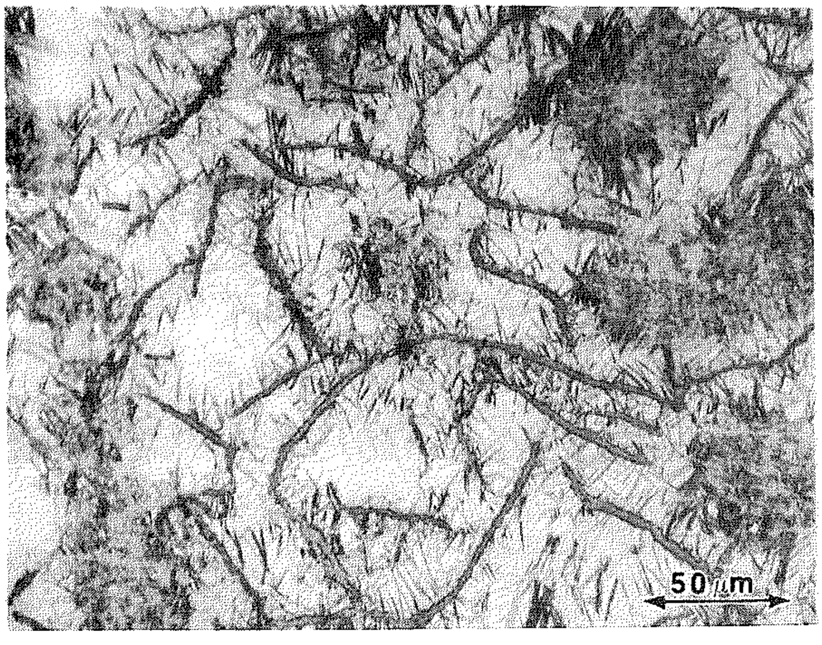

Figure 33. Middle portion of figure 30. 400x.

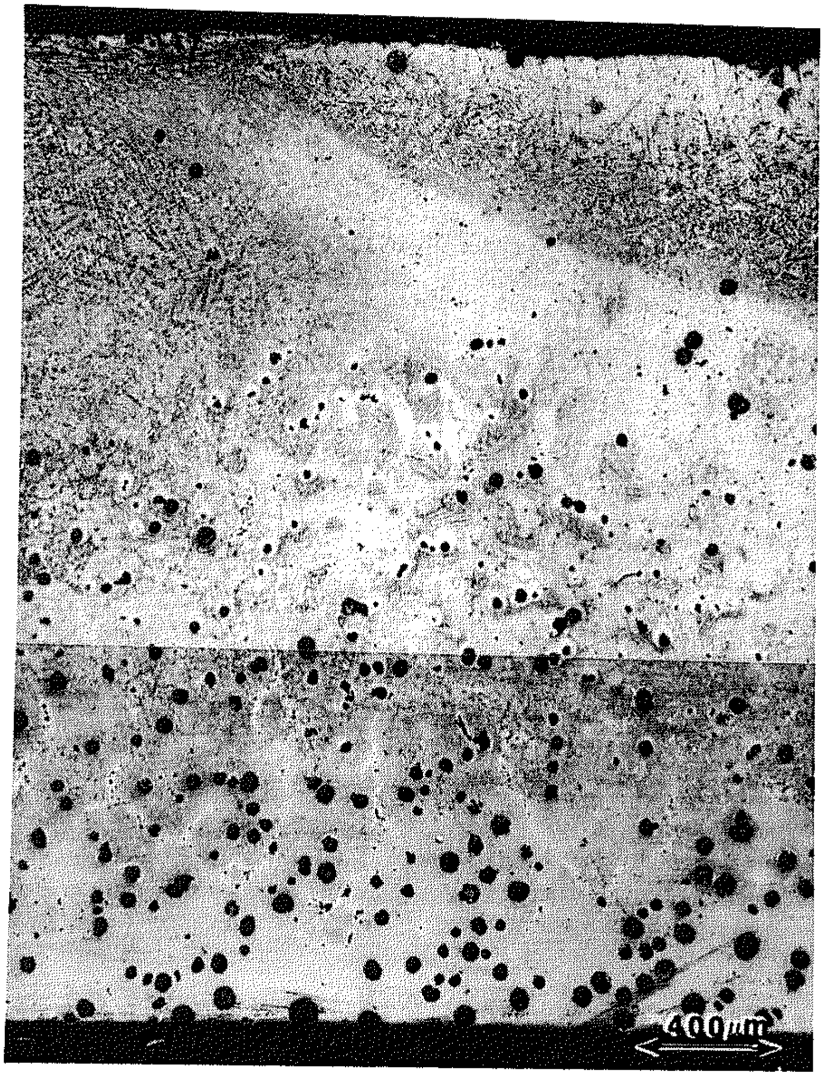

Figure 34. Microstructure of integrated beam laser processed ductile iron (2.5 kW, 0.83 cm/sec). 50x

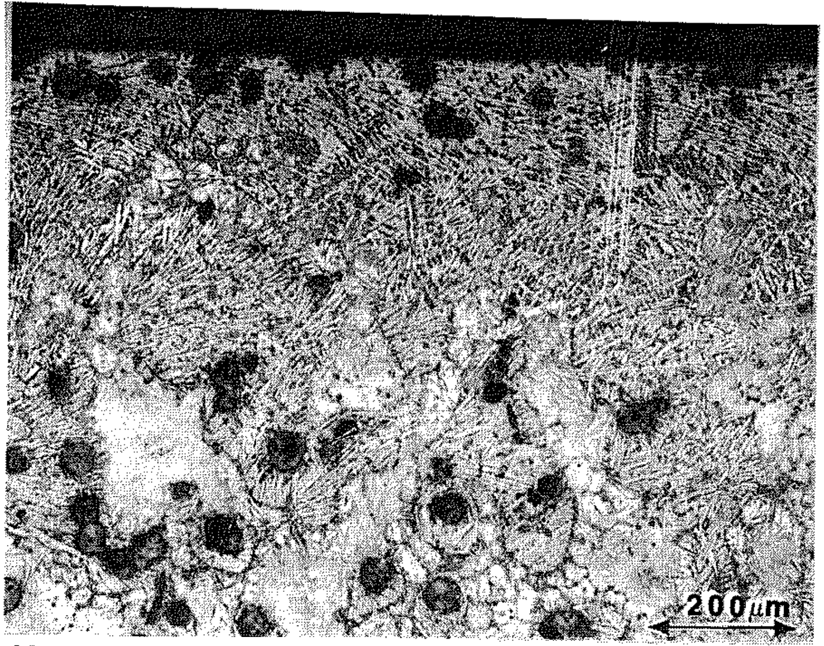

Figure 35. Same as above, at a higher magnification. 100x

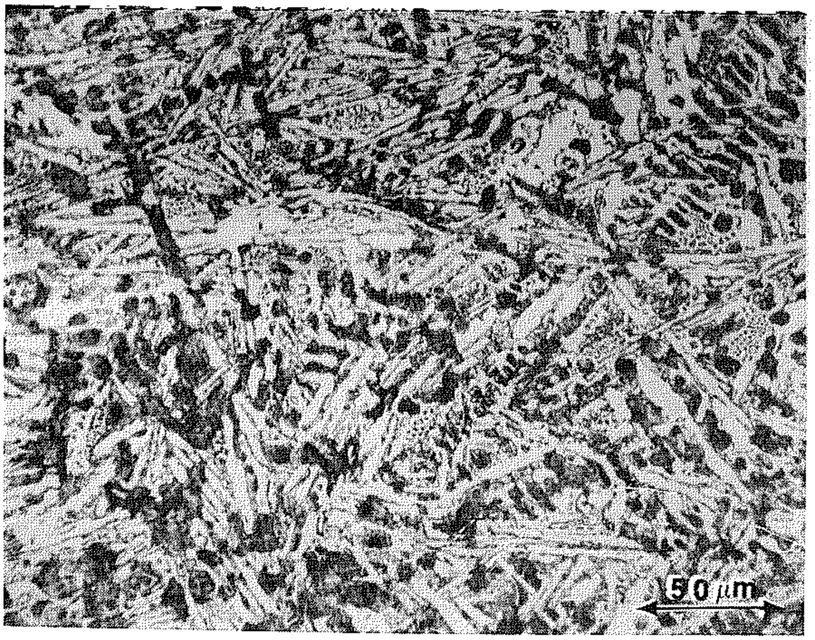

Figure 36. Same as above, at a higher magnification. 400x

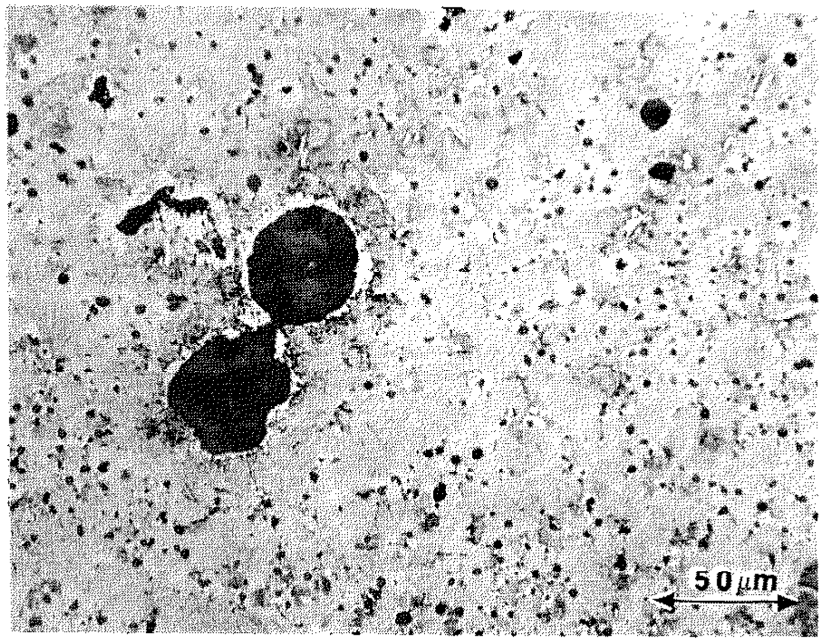

Figure 37. The white band in the upper middle portion of figure 34 (laser path overlap region). 400x

B. Slurry erosion

1. Fine particle slurry erosion

Initial slurry erosion testing was done using both a fine particle size (~ 45 μm) SiO_2 slurry, and a fine particle size (~ 60 μm) SiC slurry. The erosion rates produced with these particle sizes were too low to be useful. The results of these tests are shown in figure 38 for the as-received materials. In this, and subsequent figures, the erosion depth scale is calculated from the weight loss measurements.

2. Large particle size SiO_2 slurry erosion

AFS 50/70 mesh SiO_2, with an average particle size of 250 μm, was used to make a 35 wt.% (17 vol%) water slurry. Samples were attached (see figure 9) to the sample holder with the sample surface positioned at an angle of 45° face down and rotated at 575 RPM. SEM micrographs shown in figures 39 through 42 show the as-eroded surface features of gray cast iron samples in both the as-received and the laser processed conditions. The erosion time was 12 hours for all specimens. Figure 39 shows large erosion craters which are a little bit smaller than the size of erodant particles (~ 250 μm). At the same magnification (100x), figure 41 shows many small pits on the eroded surface, and at a higher magnification (figure 42), these pits appear to be the undeformed dendrites.

The macroscopic surface appearance of gray and ductile cast irons in both the processed and as-received conditions, after 114 hours of SiO_2 slurry erosion, are shown in figures 43 through 46. Note that in each figure one side of each sample has been cut and placed next to the remainder to show the erosion crater depth. Both as-received gray and ductile irons showed very rough surface compared to the area protected by thermosetting plastic, and a

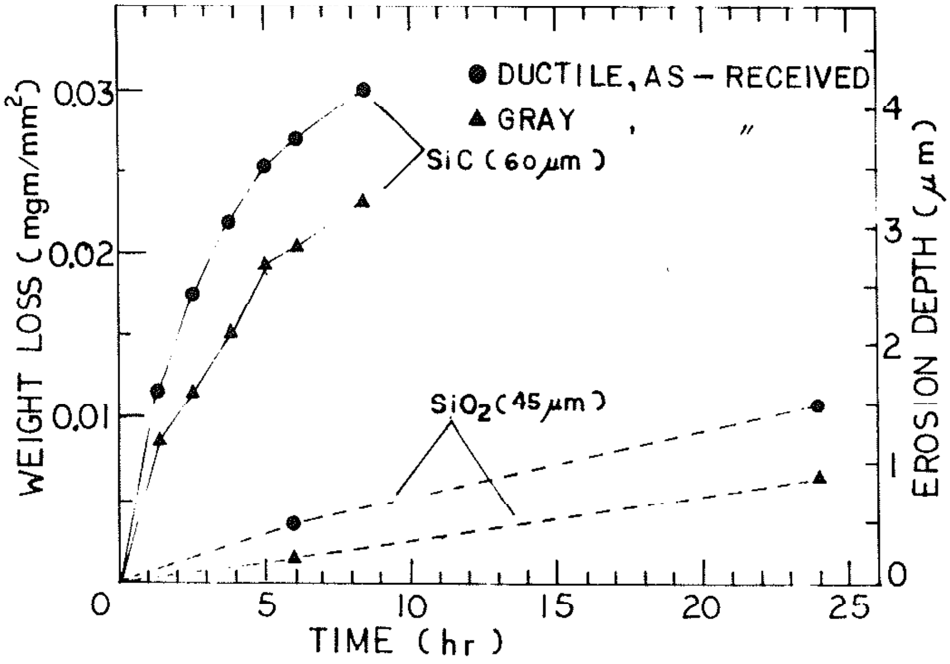

Figure 38. 66 wt.% fine particle slurry erosion of as-received cast irons.

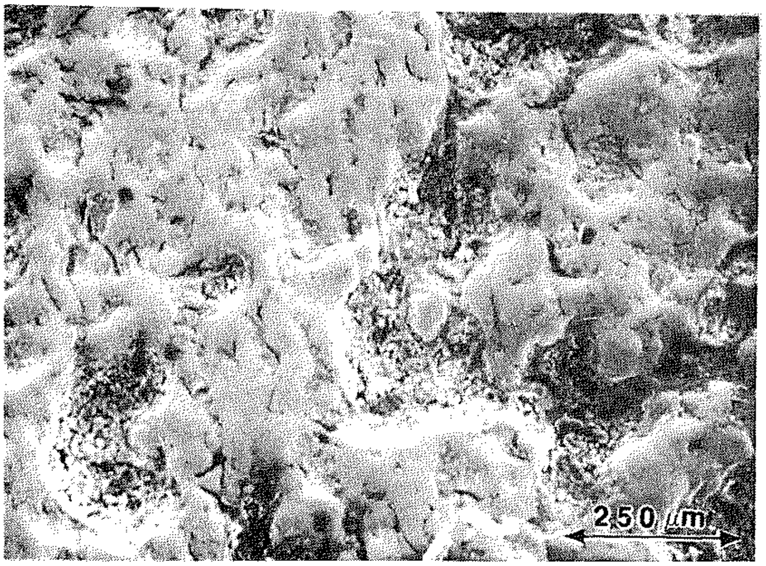

Figure 39. SEM surface feature of slurry eroded, as-received gray iron sample (12 hours SiO_2 slurry erosion). 100x

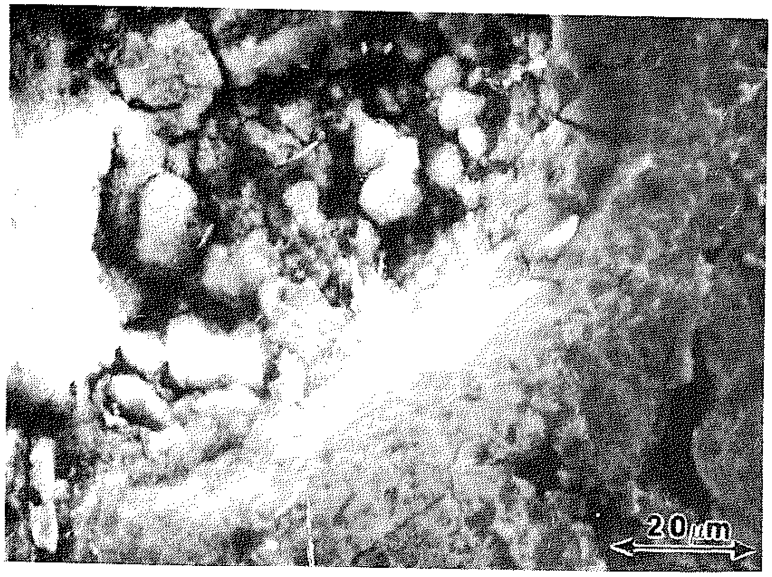

Figure 40. Same region as figure 39 at a higher magnification. 1000x

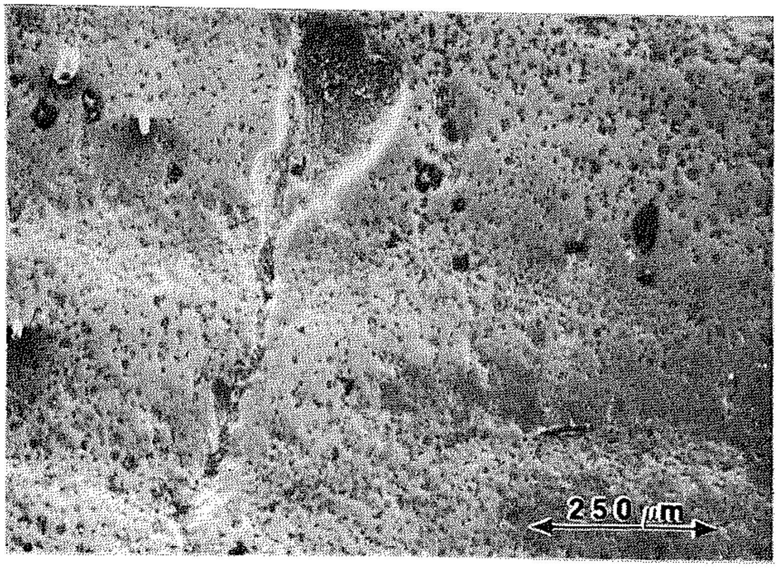

Figure 41. SEM surface feature of slurry eroded, laser processed (4 kW, 25 RPM) gray iron sample (12 hours SiO_2 slurry erosion). 100x

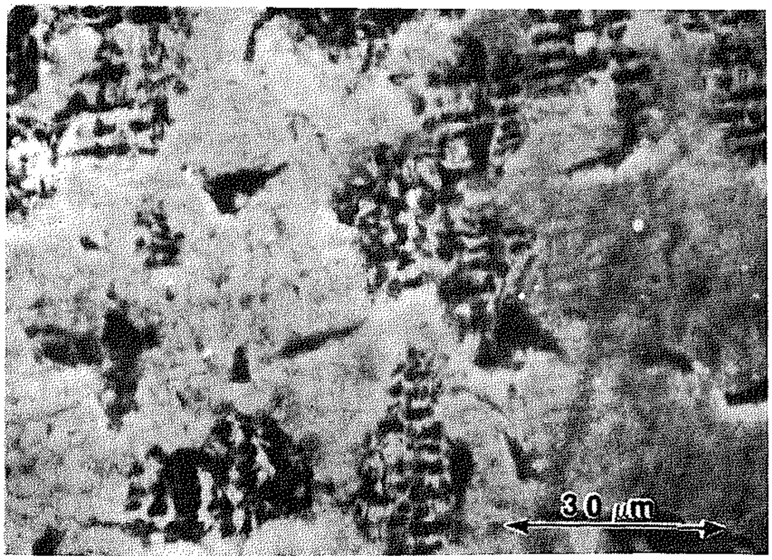

Figure 42. Same region as figure 41 at a higher magnification. 1000x

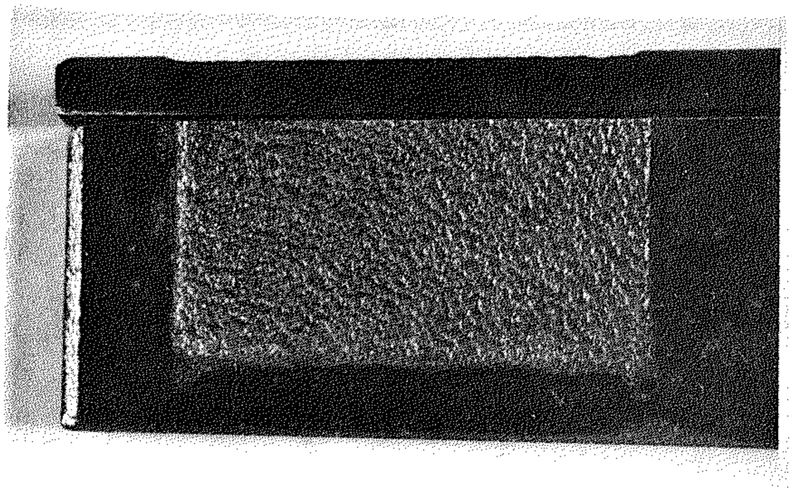

Figure 43. Surface appearance of slurry eroded as-received ductile iron (114 hours SiO_2 slurry erosion).

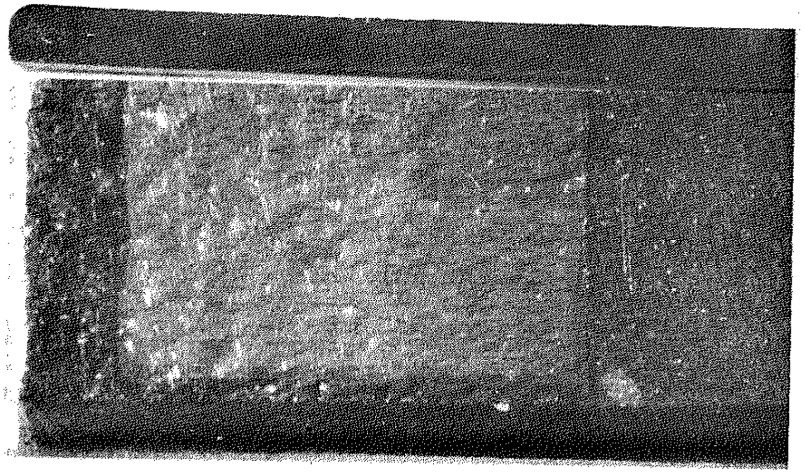

Figure 44. Surface appearance of slurry eroded laser processed (4 kW 15 RPM) ductile iron (114 hours SiO_2 slurry erosion).

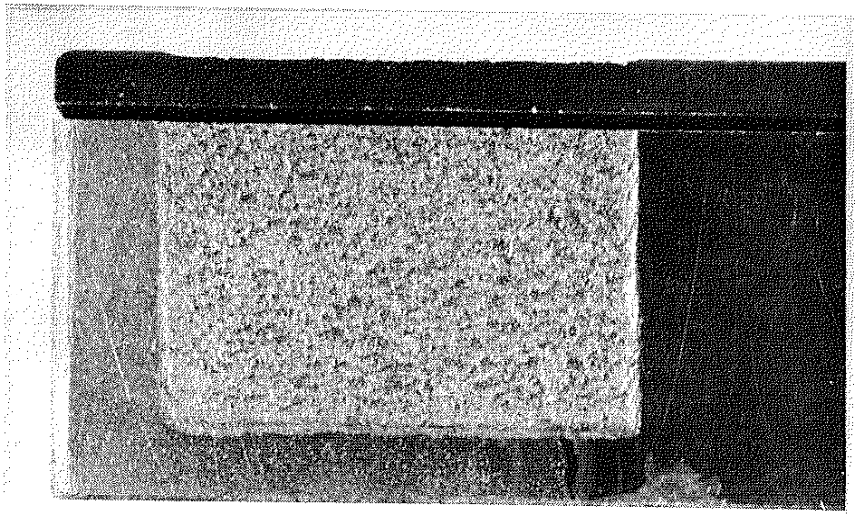

Figure 45. Surface appearance of slurry eroded as-received gray iron (114 hours SiO_2 slurry erosion).

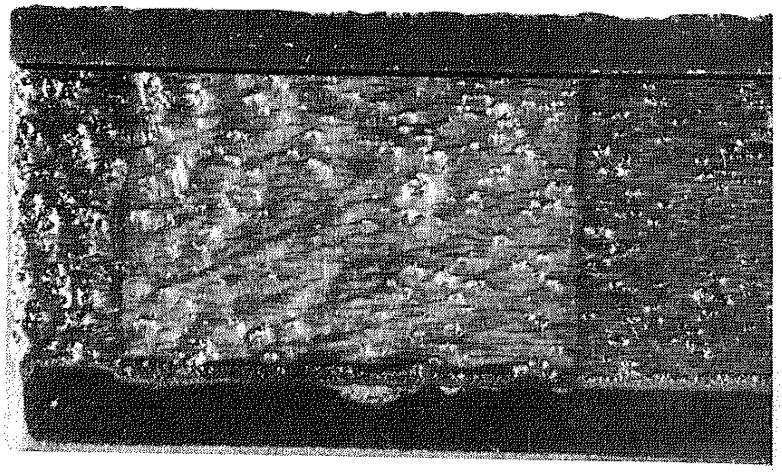

Figure 46. Surface appearance of slurry eroded laser processed (4 kW 25 RPM) gray iron (114 hours SiO_2 slurry erosion).

very deep (~ 300 μm) eroded depth. However, in the laser processed case, neither gray nor ductile irons showed significant change of their surface roughness and eroded depths were not easily detected. Figure 47 shows the surface roughness profiles of the specimens shown in figures 43 to 46. It is evident that laser processing has resulted in significant reduction in crater depth in these materials after SiO_2 slurry erosion for 144 hours.

Figure 48 shows the sectional view of low powder density mirror laser processed, SiO_2 slurry eroded gray cast iron. There is a significant difference between the eroded surface of the two microstructures shown in this figure. The top left portion is a white cast iron microstructure, which was eroded only slightly. The top right portion is a white cast iron matrix with some dark, round phase in it, and this was eroded severely.

Measurements of erosive wear in units of sample weight loss per mm^2 of eroded area and erosion depth are plotted as functions of time in figures 49 to 52. Figure 49 shows erosive wear of both gray and ductile cast iron samples, as-received and focussed beam laser processed (with a variety of laser processing conditions). After 12 hours SiO_2 slurry erosion, both as-received gray and ductile iron samples showed higher (about a factor of 2.2) weight loss than the laser processed samples. The ductile iron samples had higher weight loss than the gray iron samples in both as-received and laser processed conditions. For laser processed gray iron, the erosion resistance seemed to decrease in the following order: 3 kW 25 RPM, 4 kW 25 RPM and 4 kW 15 RPM. For laser processed ductile iron the order of decreasing resistance to erosion was : 4 kW 25 RPM, 4 kW 15 RPM and 2 kW 25 RPM.

Figure 50 shows the erosive wear of integrated beam laser processed samples of both ductile and gray irons. After 12 hours SiO_2 slurry erosion, the ductile iron laser processed samples had a higher weight loss than the

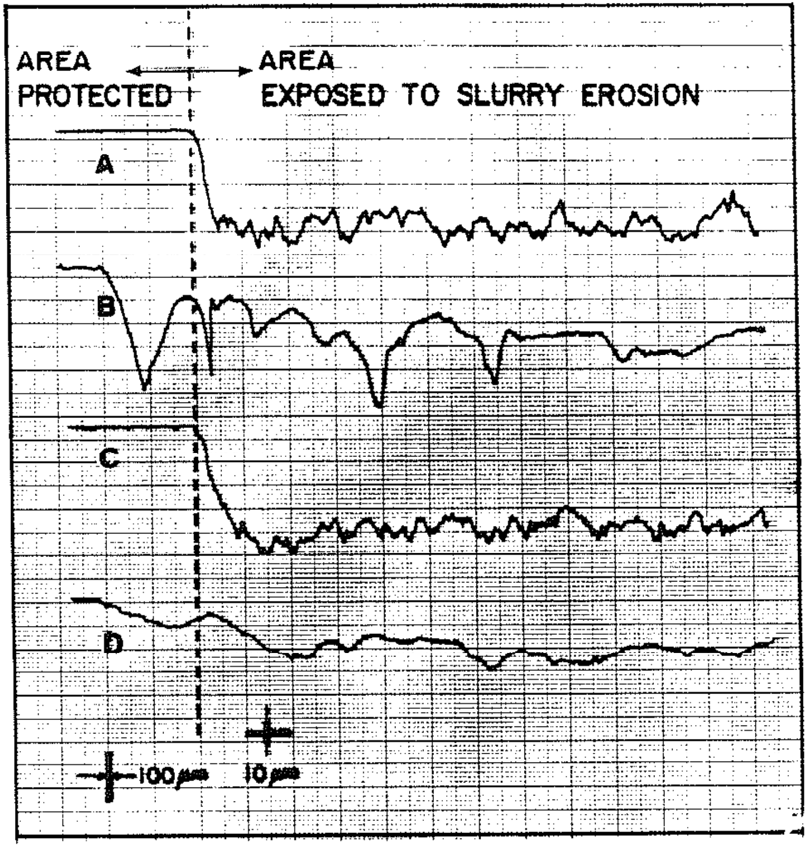

Figure 47. Surface profiles parallel to beam travel direction of eroded samples after 114 hours of SiO_2 slurry erosion.
A = as-received gray iron, surface ground before testing.
B = as-laser processed gray iron, 4 kW 25 RPM.
C = as-received ductile iron, surface ground before testing.
D = as-laser processed ductile iron, 4 kW 15 RPM.

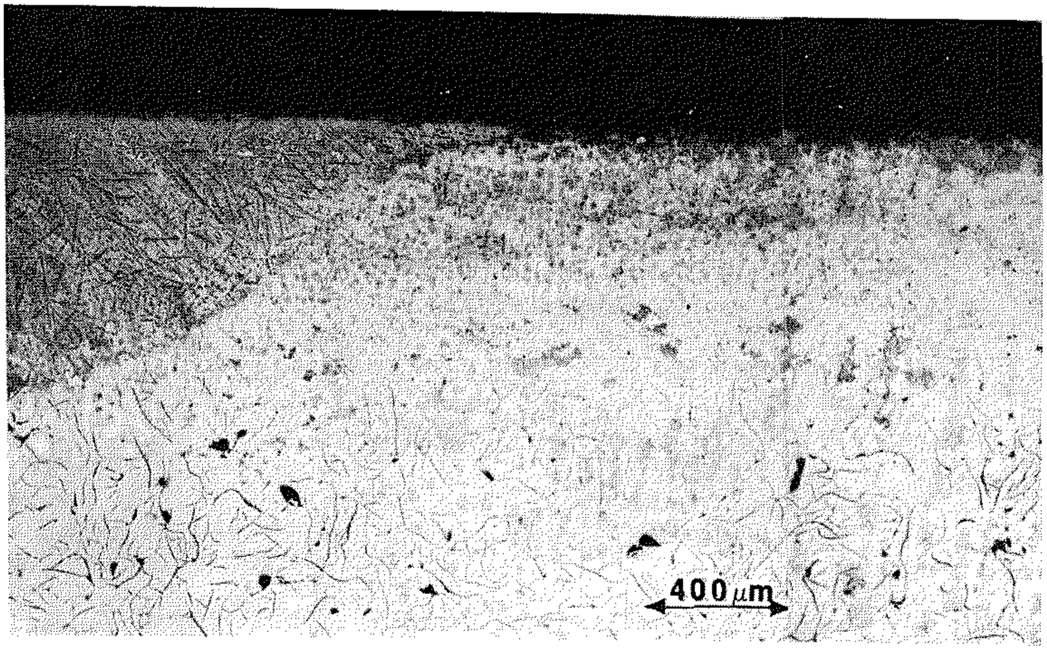

Figure 48. Sectional view of integrated beam laser processed (7 kW, 2.08 cm/sec sample speed), slurry eroded gray iron (12 hours erosion in 35 wt.% SiO_2 slurry). 50x

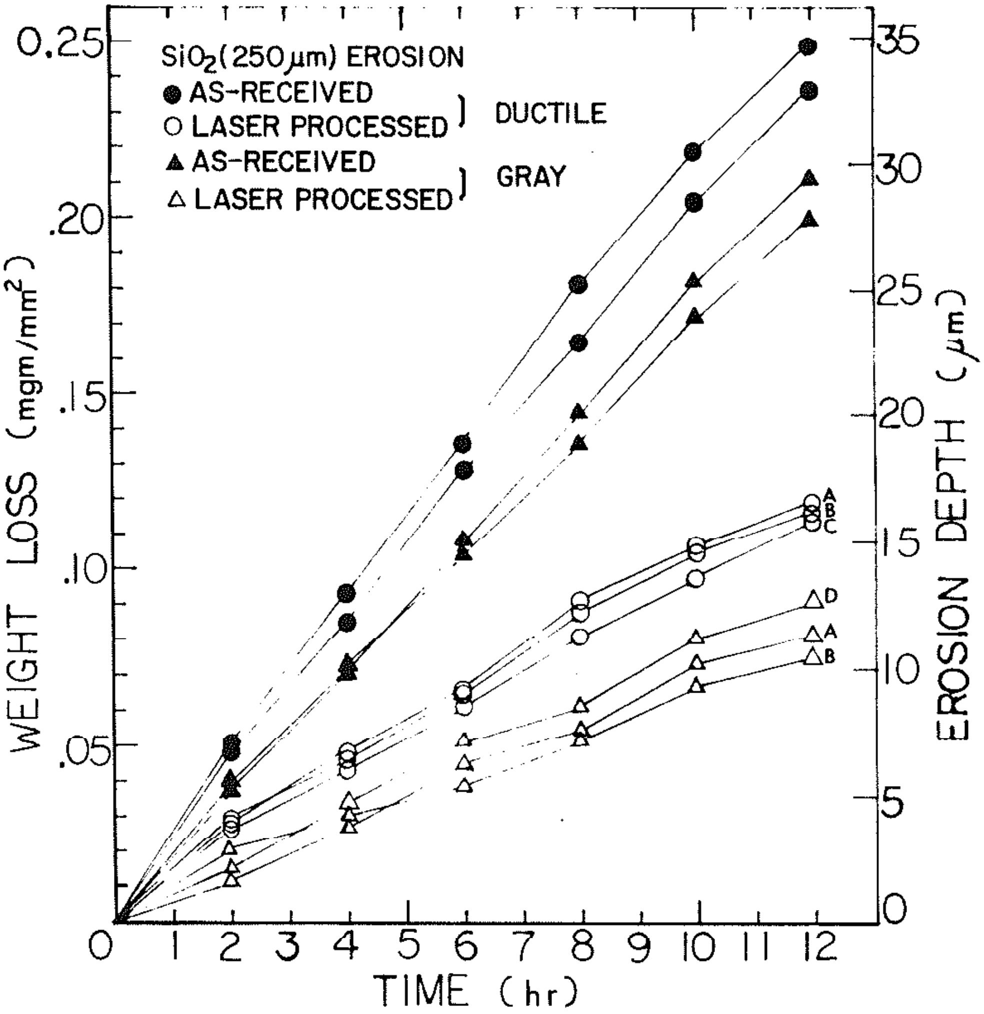

Figure 49. Erosive wear of as-received and focussed beam laser processed samples (35 wt.% SiO_2 slurry).
A = 4 kW, 15 RPM; B = 4 kW, 25 RPM; C = 3 kW, 25 RPM;
D = 2 kW, 25 RPM.

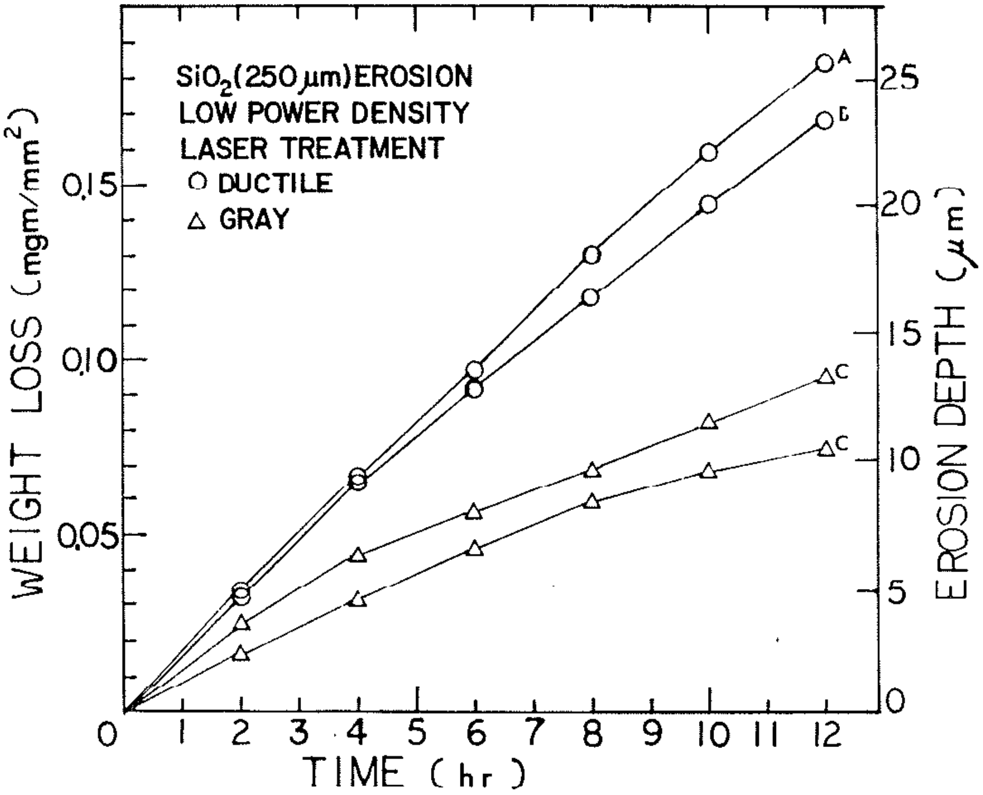

Figure 50. Erosive wear of integrated beam laser processed samples (35 wt.% SiO_2 slurry).
A = 2.5 kW, 0.83 cm/sec; B = 1.5 kW, 0.42 cm/sec;
C = 7 kW, 2.08 cm/sec.

gray iron laser processed samples. For the ductile iron, the 1.5 kW, 0.42 cm/sec sample speed processed sample seems to be more erosion resistant than the 2.5 kW 0.83 cm/sec sample speed processed one.

Figure 51 shows erosive wear of focussed beam laser processed and as-received gray and ductile iron samples by extended exposure to SiO_2 slurry erosion for times up to 114 hours. Both as-received gray and ductile iron samples have essentially the same erosion rate. The laser processed (at 4 kW 25 RPM) gray iron erosion rate is reduced by a factor of 5 relative to as-received material and the laser processed ductile iron erosion rate is reduced by a factor of 4.

Figure 52 shows the effect of surface grinding (~ 100 μm deep) after laser processing. At the same processing condition (4 kW 15 RPM), ductile iron shows a 30% improvement of erosion resistance after grinding. For gray iron at 4 kW 25 RPM, there is a 20% improvement of erosion resistance after grinding. At the same laser condition (4 kW 5 RPM), after surface grinding, the gray iron sample shows better erosion resistance than a ductile iron sample.

3. Large particle SiC slurry erosion

Figure 53 shows the results of large particle size (250 μm) SiC slurry erosion testing. All the other testing conditions except abrasives remained the same as the SiO_2 (250 μm) erosion test. Comparing figure 53 and figure 49, one finds that there is a ~ 60% increase in the erosion rate by SiC of the as-received cast irons, and ~ 30% increase in the laser processed case.

4. Corrosion-erosion

Figure 54 shows the results of corrosion-erosion testing of laser processed and as-received cast iron samples in a 37.5 wt.% SiO_2 + 0.01 N HCl

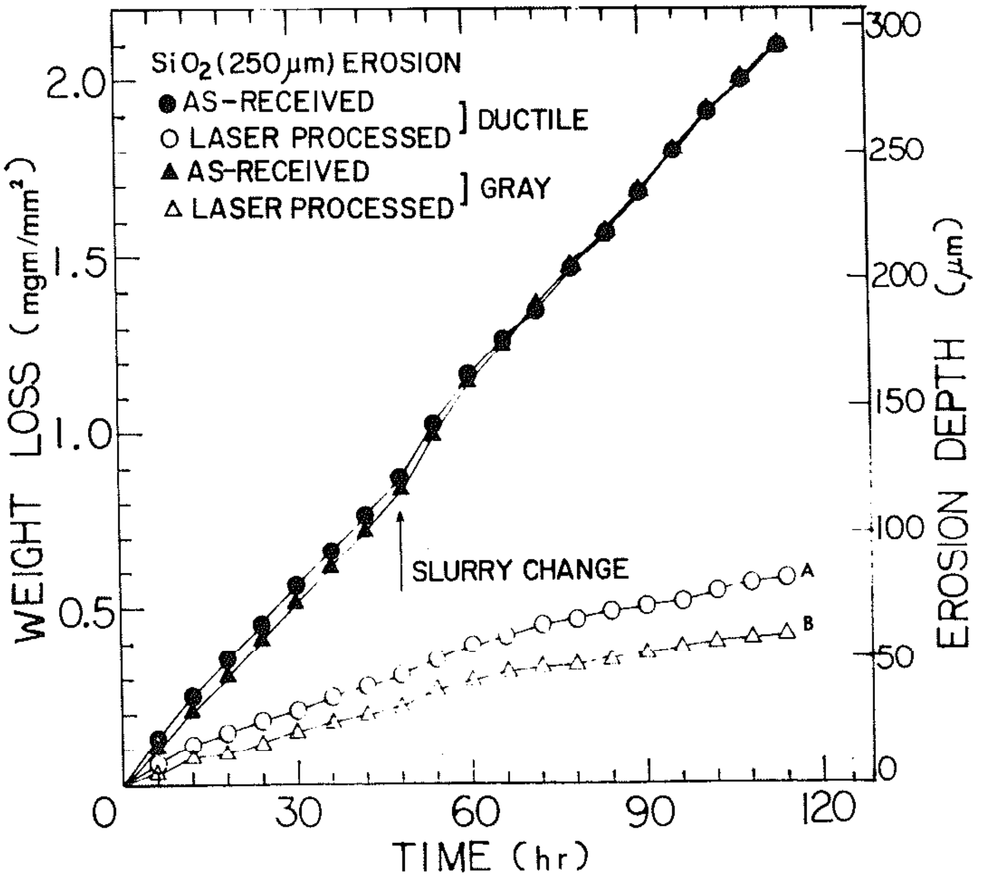

Figure 51. Extended erosive wear (35 wt.% SiO_2 slurry).
A = 4 kW, 15 RPM; B = 4 kW, 25 RPM.

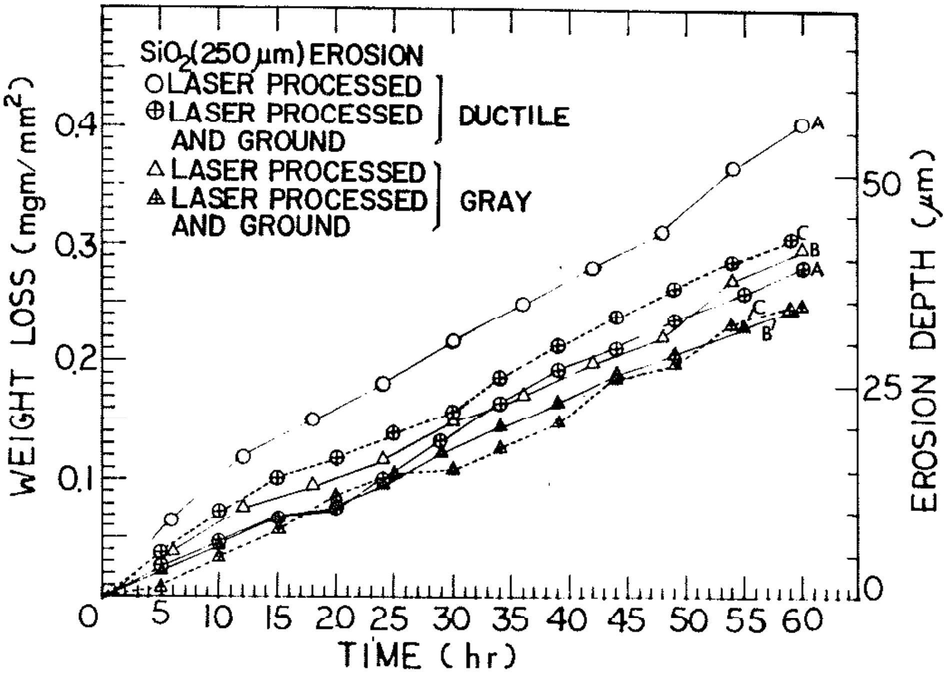

Figure 52. Effect of surface grinding on erosive wear (35 wt.% SiO$_2$ slurry). A = 4 kW, 15 RPM; B = 4 kW, 25 RPM; C = 4 kW, 5 RPM.

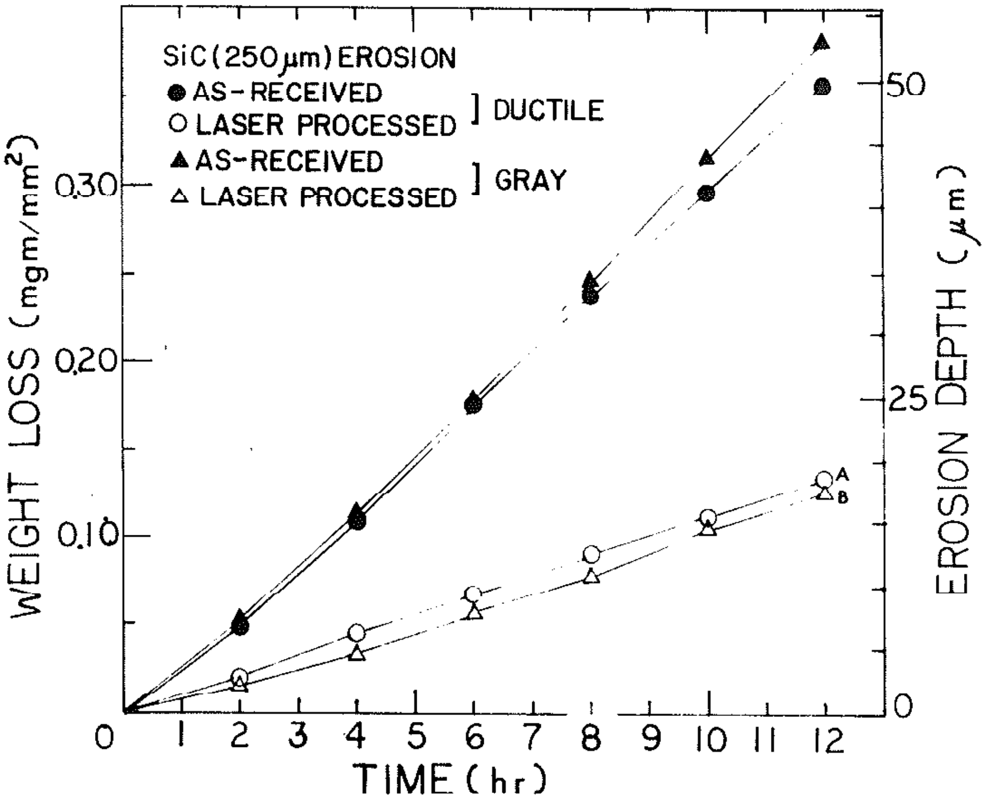

Figure 53. Erosive wear of as-received and focussed beam laser processed samples (35 wt.% SiC slurry). A = 4 kW, 25 RPM; B = 2 kW, 15 RPM.

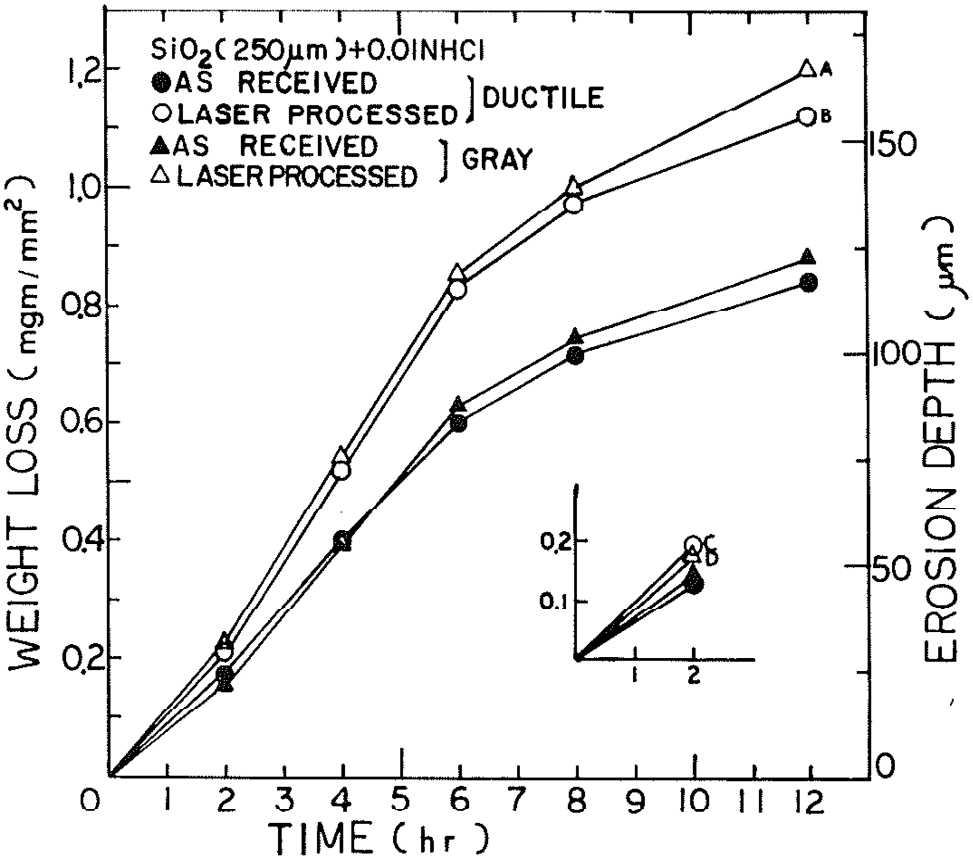

Figure 54. Corrosion-erosion of laser processed and as-received cast iron samples (37.5 wt.% SiO_2 + 0.01 N HCl slurry). A = 3 kW, 25 RPm; B = 4 kW, 25 RPM; C = 1.5 kW, 0.42 cm/sec; D = 7 kW, 2.08 cm/sec (C,D were tested in a slurry which had been used for 12 hours for A,B).

slurry. The laser processed cast iron samples show a greater weight loss after testing than the as-received cast iron samples do.

C. Airabrasion

An S.S. White model K airabrasive unit was used to measure the resistance of the material to air-entrained abrasive particles using 50 μm Al_2O_3 powder. Figure 55 shows an optical micrograph of the Al_2O_3 powder before testing.

Figures 56 and 57 show the erosion (mgm/gm abrasive) as a function of impingement angle. The bar scale used in the figures is a $\pm 2\sigma$ deviation from the average value. The particle flow rate was about 3.3 gm/min and the particle velocity was about 50 m/sec. Figures 56 and 57 show that the laser processed cast iron samples suffer even more weight loss per gram abrasive particle than the as-received cast iron samples do at angles of 30° an 90°.

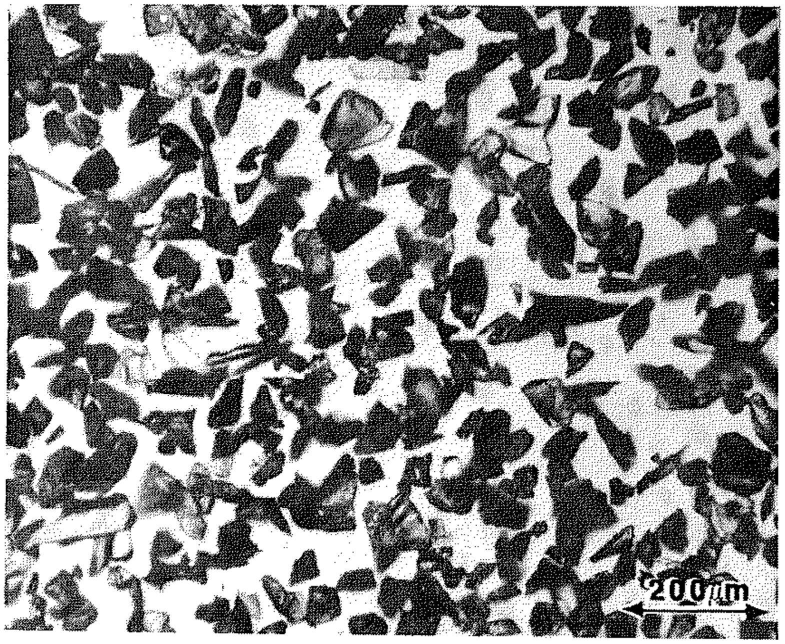

Figure 55. S.S. White #3 airabrasive powders Al_2O_3 (~ 50 μm). 100 x

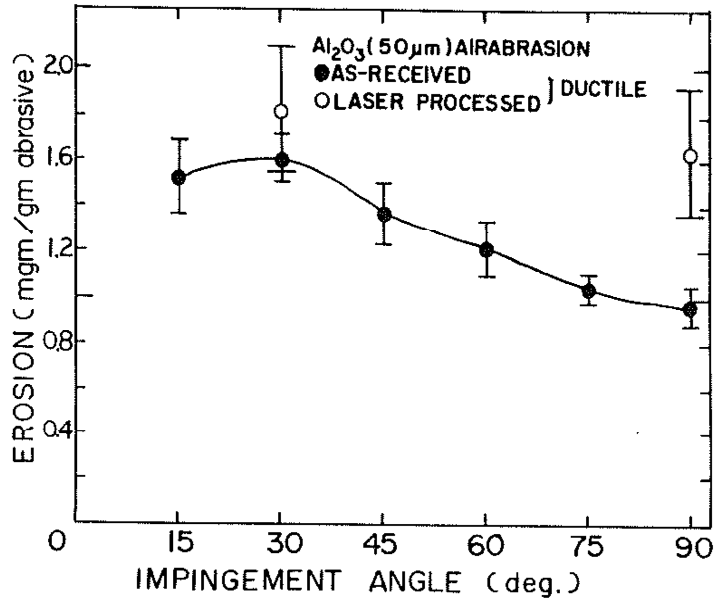

Figure 56. Airabrasion of as-received and laser processed ductile iron samples as a function of impingement angle.

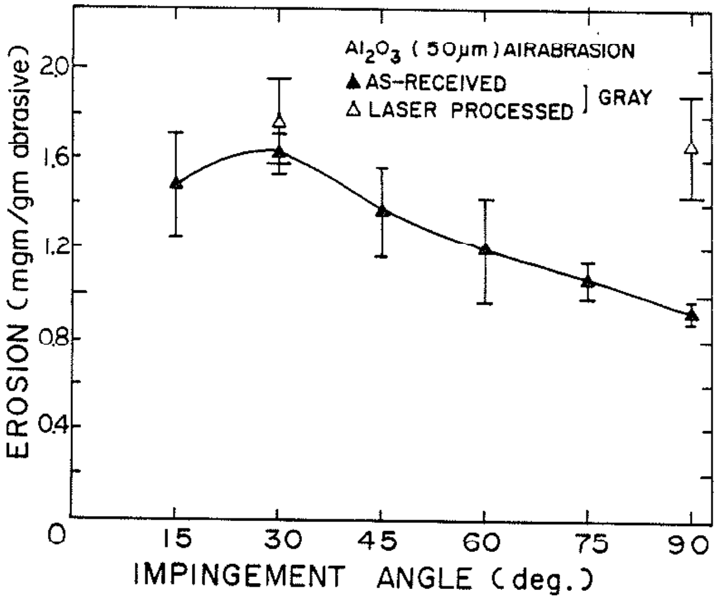

Figure 57. Airabrasion of as-received and laser processed gray iron samples as a function of impingement angle.

V. DISCUSSION

A. Laser processed microstructures and microhardness

After processing with the focussed annular laser beam, cast iron can reach a hardness as high as DPH 1245 with a hardened layer as deep as 1 mm. Suitable processing conditions were slow sample speed past the stationary beam and a rapid flow of cooling water beneath the sample. This resulted in a longer interaction time of the laser beam with the sample surface and greater superheating of the melt, followed by rapid cooling of the melt after passage through the beam (see table 2). In the case of gray iron at 1 to 4 kW laser power, both 10 RPM (8.33 cm/sec) and 2 RPM (1.67 cm/sec) yielded a high hardness (DPH 945 to 1245), while in ductile iron this was achieved only at 2 RPM and 4 kW 5RPM. These high hardness layers had a fine feathery microstructure (see figures 22 and 24). According to Hume-Rothery [43], this microstructure consists of parallel cementite plates and pearlite constituent, sometimes called plate-like eutectic. It is stronger than ledeburite. Its formation always involves supercooling. Supercooling is favored by superheating the melt, which reduces the nucleation. White irons usually are evaluted on the basis of hardness, because wear resistance normally increases with hardness. Typical hardness values of chill cast white iron range from a minimum of 550 HV to a maximum of 800 to 950 HV in a fully hardened condition (depending on retained austenite content) [44]. The high hardness (DPH 945 to 1245) obtained by this laser processing is remarkably greater than those of the conventional chill cast white iron indicating that this laser hardened layer could have an even better resistance. However, in spite of their high hardnesses, problems with severe surface cracking and macroscopic bulge-depression surface geometries have stopped further laser processing at such a slow sample moving speed.

Other focused beam laser variables were tried, (see table 2) but most of them yielded a dendritic structure (see figures 21 and 23) and intermediate hardnesses of DPH 560 to 940. From the electron (figure 26) and x-ray diffraction patterns of laser processed ductile iron (figure 29), it is apparent that most of the dendrites are austenite, which remains stable at room temperature (after 7 months since laser processing, no signs of transformation have been observed). It is found that the austenite 200 peak intensity is much stronger than the 111 peak, while in a randomly oriented austenite crystal, the 111 peak should be about twice the intensity of the 200 peak. This means there is a preferred orientation in this austenite matrix with <100> normal to the surface (parallel to the heat flow direction). X-ray analysis also shows that the austenite contained approximately 1.8 wt.% C, calculated from the following equations relating austenite lattice parameter and carbon content [45].

$$a = 3.548 + (0.044)\ x$$

This composition is consistent with the carbon content of a modestly supercooled iron of the roughly eutectic composition of the ductile iron [46]. The x-ray diffraction patterns also contained small peaks indexed as cementite, graphite and ferrite.

During the laser surface melting of ductile iron, most of the graphite nodules dissolved in the melt, except near the solid/liquid boundary, where the time and temperature were insufficient to allow dissolution. In several places graphite nodules were observed to have floated up to the surface.

For the gray iron, the existence of small pores near the solid/liquid boundary agrees with observations by Sedunov, et al. [40], who proposed that this was the result of evolution of gases absorbed by graphite during solidification of the cast iron. Based on the hardened depth, microhardness, surface roughness and cracking, 4 kW 25 RPM (20.8 cm/sec relative beam speed) and 4 kW 15 RPM (12.5 cm/sec relative beam speed) seemed to be the best focussed beam laser processing conditions for ductile cast iron and gray cast iron, respectively.

The lower power densities obtained when processing with the integrating mirror, also melted the cast iron when it moved at a relatively slow speed past the beam (0.42 - 2.08 cm/sec). There is no cooling water beneath the specimen in this case, and the specimen thickness is too thin to give a bulk self-quenching effect. After several passes, the temperature of the specimen begins to rise, and the cooling rate at the surface decreases. It has a slower cooling rate in this case than in focussed annular laser beam processing. The average hardness varies from DPH 650 to 740 (see table 4), and there is no cracking of the specimen surface.

The gray cast iron specimen processed at 7 kW, 2.08 cm/sec sample speed generally show three kinds of microstructure: in the laser melted zone, it is basically white cast iron--ledeburite eutectic and primary dendrites which were originally of austenite, and then transformed to pearlite on cooling below the A_1 point (see figure 31). It has an average hardness value of DPH 740. In the laser pass overlap region, the matrix has the white cast iron structure with some dark, round phase (possibly pearlite nodules) scattered around (see figure 32). The nature of this dark phase was not definitely known, but this whole area is softer (DPH 636, see table 4). Below the melted layer, there is a typical transformation-hardening area (see figure 33), where the matrix is martensite in austenite with graphite remaining in flake shapes. This area has an average hardness of DPH 490.

The ductile iron also showed three kinds of structures, the white cast iron structure (figure 36), the martensite-austenite structure (see figure 35) and in the overlap region, a bainite matrix with very fine and uniformly dispersed graphite particles (see figure 37). The average hardness in this overlap region is DPH 361. In figure 35, the floating of graphite nodules towards the top surface of the melted region can be clearly seen.

B. Slurry erosion

1. Particle size effect

Comparing figures 38 and 49, one finds that erosion rate increases substantially with increasing erodant particle size, in agreement with observations of Jackson [28]. The main reason is that as the particle size is increased, it obtains more kinetic energy and thus higher stresses are applied to the specimen surface upon particle impact.

2. Laser processed vs. as-received cast iron

In every test in neutral slurries, the laser processed cast irons are much more erosion resistant than the as-received cast irons (see figures 49, 51 and 53). Figure 51 shows that in an extended erosion test (114 hours exposure) the laser processed gray cast iron erosion rate is reduced by a factor of 5 relative to as-received material and the laser processed ductile iron erosion rate is reduced by a factor of 4. This improvement in erosion resistance is better than the factor of 3 observed by

Golubets et al. [37], and worse than the factor of 10 obtained by Wineman et al. [30]. However, Wineman et al. were mainly interested in laser processing ferritic malleable iron. The normal hardness range for this material is very low (BHN 116 to 156) and the wear resistance of it is very poor. Nodular iron with hardness ranging from BHN 156 to 229 can have a better wear resistance up to a factor of 10 compared to this material [30]. This may explain why their laser processing showed a larger improvement in wear resistance than did ours.

The main reason for this improvement in slurry erosion resistance is the high hardness of the processed layer. Figures 39 to 42 show the difference between the eroded surfaces of as-received and laser processed gray cast iron specimens. Figure 39 shows large erosion craters which are a little bit smaller than the size of erodant particles (~ 250 μm), while at the same magnification (100x), figure 41 shows many small pits on the eroded surface, and at a higher magnification (figure 42), these pits appear to be the undeformed dendrites. This means there are two different erosion mechanisms involved in this experiment. First, in an as-received cast iron sample, because it is relatively soft and ductile (HRB 90), it is a cutting-gouging mechanism. Second, in a laser processed specimen, because it is hard and brittle, the erodant particles cannot cut into the surface, instead, they tend to deform the surface to the point of fracture; i.e., it is a deformation-fracture mechanism. These photos (figures 39 to 42) agree very well with the abrasive wear theory proposed by Moore et al. [12] and Bitter [29].

3. Laser processing variables

Figures 49 and 50 show the effects of different laser processing variables. Under the same laser processing conditions, gray iron specimens have better erosion resistance because they have higher hardnesses than the ductile iron specimens (see table 2). Ductile iron specimens have a small number of graphite nodules floated to the top. This would undoubtedly degrade erosion resistance. In focussed beam laser processed ductile iron (figure 49), all three laser treatments yield roughly the same hardness (~ DPH 660), but as the power input increases and the sample speed slows down, there appear to be more surface cracks. This may explain why curve C (3 kW, 25 RPM) is better than curve A (4 kW, 15 RPM), because it is much weaker and more sensitive to the particle impacts around the cracks (see the top of figure 41, where a large chip near the crack broke off), although they differ only slightly in the total weight loss. In figure 50, the low power density processed ductile iron shows much worse resistance than for focussed beam laser processing, however, it is still better than the as-received ductile iron. The major reason for this difference seems to be the larger number of graphite nodules at the surface and the much softer laser pass overlap area in the integrating mirror case. The erodant particles can easily erode the softer phases away, and speed up the whole erosion process. Again in the focussed beam laser processed gray iron (figure 49), the hardness and surface cracking decide the erosion resistance, in this case, the 4 kW 25 RPM laser processing seems to be the best.

There is no significant difference between the erosion resistance of focussed beam and integrated beam laser processed gray iron samples. However, there is one thing worth mentioning here. As discussed earlier, in the laser pass overlap region of the integrated beam laser treatment there exists a softer dark phase. During erosion this dark phase seems to be vulnerable to particle attack, and the whole overlap region appears to wear more severely than the nearby white cast iron layer (see figure 48).

4. Surface grinding effect

Figure 52 shows the effect of surface grinding (~ 100 μm deep ground away). Ductile iron shows a ~ 30% improvement after grinding, while gray iron shows an improvement of about 20%. The reason that ductile iron shows a larger amount of improvement seems to be the removal of surface graphite nodules. Again, in figure 52, hardness and surface cracking play an important role in erosion resistance.

5. SiC vs. SiO_2

Comparing figures 53 and 49, one finds that there is a ~ 60% increase in the erosion rate by SiC of the as-received cast irons, and ~ 30% increase in the laser processed case, all the other testing conditions except abrasives remained the same as the SiO_2 (250 μm) erosion test. The increase in the erosion rate by SiC is not only due to the increase in hardness (SiO_2 = 1200 kg/mm^2, SiC = 3000 kg/mm^2) and angularity (see figures 10 and 11) but also to an increase in density relative to SiO_2 (SiC = 3.2 gm/cm^3, SiO_2 = 2.6 gm/cm^3). This agrees with results of Levy et al. [27].

In an article by Zum-Gahr [14], it is discussed that under test conditions of low stress abrasion with an abrasive softer than the iron carbides, wear resistance of chromium alloyed white cast irons has been shown to decrease with increasing retained austenite content. However, retained austenite has been found favorable for wear resistance in white cast irons abraded by an abrasive harder than the iron carbides. In general, the loss of hardness attributed to retained austenite can be compensated for by an increase in work hardening rate of this phase. This may explain why the relative increase of erosion rate by SiC over SiO_2, of laser processed cast irons (containing large amounts of austenite) is only half of that of as-received cast irons.

6. Corrosion-erosion

The corrosion-erosion testing results of laser processed and as-received cast iron specimens in a 37.5 wt.% SiO_2 + 0.01 N HCl slurry are shown in figure 54. Here the laser processed cast iron samples show a greater weight loss after testing than do the as-received cast irons. The reason for this may be corrosive attack of laser processed cast iron along the surface cracks and weak interdendritic regions deep into the hardened substrate, while the corrosion-erosion of as-received cast iron can only erode away the substrate layer by layer. This is rather speculative and the actual reason for the poorer behavior of laser treated specimens needs further investigation. The corrosion-erosion rate of laser processed and as-received cast irons are about 12 times and 4 times faster, respectively, than the erosion rates in the same slurry without the addition of HCl.

C. Airabrasion

The Al_2O_3 particle with an average size of 50 μm was used to measure airabrasion resistance. The particle flow rate was about 3.3 gm/min, and the particle velocity was about 50 m/sec. Figures 56 and 57 show that the laser processed cast iron samples suffer even more weight loss per gram abrasive particles than do the as-received cast iron samples at angles of 30° and 90°. As observed by Finnie [29], fully hardened 1055 steel shows more erosion loss than the as-received 1055 steel at angles higher than 30°. This was explained for a pearlitic microstructure based on a mechanism of material loss where the material could be driven from the surface in the form of chips that have cracked from the surface along brittle cementite lamellae. Within limits, the more continuous the ferrite matrix, the lower the erosion rate will be [47]. It appears that the same thing happens here. As the cast irons are laser hardened, they become more brittle and cracks from the surface form chips very easily, resulting in a higher weight loss.

VI. CONCLUSIONS

1. After processing with the focussed laser beam, cast iron can reach a hardness as high as DPH 1245, with a hardened layer as deep as 1 mm. There are two basic kinds of microstructures produced: 1) a feathery (plate-like eutectic) structure with hardness as high as DPH 1245; and 2) a dendritic structure with an intermediate hardness ranging from DPH 560 to 940. The dendritic structure can be obtained by processing with an effective short beam dwell time for high cooling rates. The feathery structure can be obtained at the lower cooling rates caused by high power imput. However, in spite of the high hardnesses of the feathery microstructures, problems with severe surface cracking and macroscopic bulge-depression surface geometries has stopped further examination of their wear properties.
2. The dendritic structure produced by the focussed beam laser processing has a very fine dendrite arm spacing of approximately 2 μm. The matrix consists of mostly retained austenite, with small amounts of cementite and ferrite. There is a preferred orientation in the austenite matrix with <100> normal to the surface (parallel to the heat flow direction).
3. In integrated beam laser processing, the cooling rate is slower than that in the focussed beam processing due to the higher heat imput and longer effective dwell time. There is no observed cracking of the specimen surface. The average hardness ranges from DPH 650 to 740. The microstructure generally consists of white cast iron structure (i.e., ledeburite eutectic and primary dendrites which were originally of austenite and then transformed to pearlite) martensite-austenite structure and a weaker beam overlapping area.

4. In an extended SiO_2 slurry erosion test (114 hours testing time), the laser processed gray cast iron erosion rate is reduced by a factor of 5 relative to as-received material and the laser processed ductile iron erosion rate is reduced by a factor of 4. The main reason for this improvement in slurry erosion resistance is the high hardness of the processed layer. At about the same hardness, the sample with more surface cracks or surface graphite nodules showed a higher erosion rate.
5. At the same laser processing conditions, gray iron specimens have better erosion resistance, possibly because they have higher hardnesses than the ductile iron specimens while the latter have some small amount of graphite nodules at the surface. After surface grinding, ductile iron shows a ~ 30% improvement of erosion resistance, while gray iron shows an improvement of ~ 20%. The reason that ductile iron shows a larger amount of improvement seems to be the removal of surface graphite nodules.
6. After corrosion-erosion testing in a 0.01 N HCl SiO_2 slurry, the laser processed cast iron samples show a greater weight loss than the as-received cast iron samples. The resistance of the laser processed cast iron samples to air-entrained Al_2O_3 particles is also lower than that of the as-received cast irons. These two undesirable characteristics should be further studied.

REFERENCES

[1] C.D. DesForges, "Laser Heat Treatment", Tribol. Int., 11(2), p. 139-143 (1978)

[2] Thermophysical Properties of Matter; Vol. 7, edited by Y.S. Touloukian and D.P. DeWitt, IFI/Plenum, New York, p. 329 (1970)

[3] Lasers, operation, equipment, application, and design, Coherent, Inc. Engineering Staff. P. 103 (1980)

[4] C.W. Draper, "Laser Surface Alloying: The State of the Art", J. of Metals, 34(6), p. 24-32 (1982)

[5] G. Schaffer, "Lasers in Metalworking", Lasers in Modern Industry, Society of Manufacturing Engineering, p. 3-16 (1979)

[6] E.V. Locke and R.A. Hella, "Metal Processing with a High Power CO_2 Laser", J. Quantum Electronics, Vol. QE10, (No. 2), p. 179-185 (1974)

[7] K. Stanford, "Lasers in Metal Surface Modification", Metallurgia, Vol. 47, No. 3, p. 109-116 (1980)

[8] D.A. Rigney, Fundamentals of friction and wear of materials, American Society for Metals, p. 1-12 (1981)

[9] E. Rabinowicz, Friction and wear of materials, John Wiley and Sons Inc., New York, p. 109-115 (1965)

[10] L.E. Samuels, E.D. Doyle and D.M. Turley, "Sliding wear mechanisms", Fundamentals of friction and wear of materials, American Society for Metals, p. 13-41 (1981)

[11] J.F. Archard, J. Appl. Phys. 24, p. 981 (1953)

[12] M.A. Moore, "Abrasive Wear", Fundamentals of friction and wear of materials, American Society for Metals, p. 73-118 (1981)

[13] A.G. Evans, T.R. Wilshaw, "Quasi-static Particle Damage in Brittle Solids-I. Observations, Analyses and Implications", Acta Met. 24, 939 (1976).

[14] Karl-Heinz ZumGahr, "How Microstructure Affects Abrasive Wear Resistance", Metal Progress, Vol. 116, No., 4, Sep., P. 46-52 (1979)

[15] M.M. Khruschov, "Principles of Abrasive Wear", Wear, 28, pp. 69-88 (1974).

[16] R.C.D. Richardson, "The Maximum Hardness of Strained Surfaces and the Abrasive Wear of Metals and Alloys", Wear 10, pp. 353-382 (1967).

[17] K.H. ZumGahr, "Friction and Wear of a Precipitation Hardenable Austenitic Steel under Abrasive Conditions" (in German), Z. Metallkde 68, pp. 381-389 (1977).

[18] H. Berns, "Verschleissminderung durch Karbidreich Stahle", VDI-Berichte, Nr. 194, pp. 95-102 (1973).

[19] K. Rohrig, "Gefuge und Bestandigkeit gegen Mineralverschleiss con Carbidischem Gusseisen", Giesserei 58, pp. 697-705 (1971).

[20] K.H. ZumGahr, "Abrasive Wear Resistance of Ductile Iron with Different Secondary Structure" (in German), Arch. Eisenhuettenwes 50 (1979).

[21] J.M. Link and C.O. Tuason, "Pipe wear in hydraulic transport of solids", Min. Congr. J., July, 38-44 (1972).

[22] J. Postlethwaite, E.B. Tinkler and M. Hawrylak, "Corrosion studies in slurry pipelines", in N.G. Coles and S.K. Hemmings (eds.), Proc. 2nd Int. Conf. on Hydraulic Transport of Solids in Pipes, September (1972), BHRA Fluid Engineering, Cranfield, 1972, Section G2, pp. 15-24.

[23] I. Tarjan and E. Debreczeni, "Theoretical and experimental investigation on the wear of pipeline caused by hydraulic transport", in N.G. Coles and S.K. Hemmings (eds.), Proc. 2nd Int. Conf. on Hydraulic Transport of Solids in Pipes, September (1972).

[24] D.R. Bomberger, "Hexavalent chromium reduces corrosion in coal-water slurry pipelines", Mater. Prot., January 43-49 (1965).

[25] R.L. Gandi, B.L. Rickes and T.C. Aude, "Control of corrosion-erosion in slurry pipelines", in J.A. Clarke and N.G. Coles (eds.), Proc. 1st Int. Conf. on the Internal and External Protection of Pipes, September (1975), BHRA Fluid Engineering, Cranfield, 1975, Section G4, pp. 39-52.

[26] J.D. Swan, D.R. Bomberger and G.I. Barthauer, "Corrosion control achieved on coal slurry pipeline", Mater. Prot., September 26-34 (1963).

[27] A.V. Levy, W. Tsai, "Experimental measurement of accelerated erosion in a slurry pot tester," Wear 68, 289 (1981)

[28] L.D.A. Jackson, "Slurry Abrasion", Symposium on the Wear of Materials, Annual General Meeting, Ottawa, March, 1967, Trans. Vol. LXX, p. 219-224 (1967)

[29] J.G.A. Bitter, "A Study of Erosion Phenomenon, Part I and II", Wear, Vol. 6, No. 1, p. 5-21 (1963) and Wear, Vol. 6, No. 3, p. 169-190 (1963)

[30] J.A. Wineman and J.E. Miller, "Production Laser Hardening", SME Technical paper IQ77-372 (1977)

[31] M. Yessik and R.P. Scherer, "Practical Guidelines for Laser Surface Hardening", Lasers in Modern Industry, Society of Manufacturing Engineers, p. 139-146 (1979)

[32] D. Belfote, "High Power Laser Surface Treatment", Lasers in Modern Industry, Society of Manufacturing Engineers, p. 128-138 (1979)

[33] P.J. Quirk, "Laser Hardening of Diesel Engine Cylinder Bores", General Motors Institute Technical Report, Aug. (1978)

[34] L.I. Mirkin, Physical Basis of Treatment of Materials with Laser Beams (in Russian), Moscow State Univ. (1975)

[35] L.I. Mirkin, "Contact Melting at the Ferrite-Graphite Boundary under the Influence of Light Pulses from a Laser", Fiz. Khim. Obrab. Mater., No. 1, 143 (1973).

[36] V.E. Arkhipov, A.N. Grechin and M.L. Khina, "Laser Hardening of Ferritic Malleable Iron", Metal Science and Heat Treatment, Vol. 22, Nos. 3-4, p. 248-250 (1980)

[37] V.M. Golubets, M.I. Moisa, Yu.I. Babei, and G.V. Plyatsko, "Effect of Laser Treatment on the Wear of Parts in Abrasive-Oil Medium", Soviet Materials Science, Vol. 8, No. 4, July-Aug., p. 505-506 (1972)

[38] A.A. Zhukov, M.A. Krishtal, A.N. Kokora, Yu.I. Davydov and I.A. Goncharenko, "Transformations in Cementite on High-Speed Heating and Quenching", Russian castings production, May, p. 209-211.

[39] R. Brigham et al., J. of the Physics and Chemistry of Solids, Vol. 1 (1967)

[40] V.K. Sedunov, V.M. Andriyakhin, N.T. Chekanova, and V.M. Belov, "Changes in the Structure and Properties of Cylinder Sleeves of Internal Combustion Engines After Laser Treatment", Metal Science and Heat Treatment, Vol. 22, Nos. 9-10, p. 630-634 (1980)

[41] R.L. Snezhnoi, A.A. Zhukov, and A.N. Kokora, "Formation of Amorphous Phase in Cast Iron", Metals Science and Heat Treatment, Vol. 22, Nos. 11-12, p. 900-901 (1980)

[42] M.L. Capp, "Microstructure and Abrasive Wear Studies of a Laser Processed Plasma Sprayed Coating", University of Illinois, M.S. Thesis, p. 6-13 (1980)

[43] W. Hume-Rothery, The Structures of Alloys of Iron, p. 320-321 (1966)

[44] Metals Handbook, 9th ed. Vol. 1, pp. 86-87 (1978)

[45] C.S. Roberts, Trans. AIME, 191, p. 203 (1953)

[46] Metals Handbook, 8th ed. Vol. 8, p. 414 (1973).

[47] A.V. Levy, "The solid particle erosion behavior of steel as a function of microstructure", Wear 68, p. 269-287 (1981)